Quaternary Science Reviews 200 (2018) 237–252

Contents lists available at ScienceDirect

Quaternary Science Reviews

journal homepage: www.elsevier.com/locate/quascirev

Climate history of the southwestern United States based on Estancia Basin hydrologic variability from 69 to 10 ka

Kirsten M. Menking [a, *], Victor J. Polyak [b], Roger Y. Anderson [b], Yemane Asmerom [b]

[a] Department of Earth Science and Geography, Vassar College, Poughkeepsie, NY, 12604, USA
[b] Department of Earth and Planetary Sciences, University of New Mexico, Albuquerque, NM, 87131, USA

ARTICLE INFO

Article history:
Received 17 May 2018
Received in revised form
15 August 2018
Accepted 19 September 2018
Available online 9 October 2018

Keywords:
Quaternary
Paleoclimatology
Paleolimnology
North America
Sediment mineralogy (incl. clay minerals)
Estancia basin
Hydrologic balance index
Younger Dryas
Bølling/Allerød
Extrapolar climate reversal

ABSTRACT

Newly acquired U–Th dates on gypsum sands contained within Pleistocene lake sediments allow us to extend the record of climatic change in the Estancia Basin of central New Mexico back to ~69 ka from a previous limit of ~29 ka. Using a hydrologic balance index (HBI) that reflects variations in sediment mineralogy and bedding characteristics, we find strong similarities to speleothem oxygen isotopic records for the southwestern United States as well as to isotopic variations in Greenland ice cores. Intervals of wetter climate in the Estancia Basin generally appear to correlate to colder conditions in the North Atlantic and conversely. The existence of a pronounced dry period from 18.1 to 17 ka matches in timing the Extrapolar Climate Reversal of Asmerom et al. (2017) at Fort Stanton cave in southern New Mexico and confirms a different origin for this stadial-like event. Furthermore, the new U–Th dates support the existing Estancia Basin interpretation of a dry Bølling/Allerød followed by a wet Younger Dryas, a result consistent with speleothem and wet meadow evidence from New Mexico and Arizona (Asmerom et al., 2010, 2017; Polyak et al., 2004; Hall et al., 2012; Wagner et al., 2010) but in conflict with an interpretation of speleothem evidence from central Texas (Feng et al., 2014).

© 2018 Elsevier Ltd. All rights reserved.

1. Introduction

Late Pleistocene and Holocene climatic history of the southwestern United States of America (SW USA) is complex, reflecting combined influences of atmospheric reorganizations brought about by the growth and decay of the Laurentide ice sheet (Kutzbach and Wright, 1985; Benson et al., 1990; Menking et al., 2004), decadal to orbital-scale changes in solar radiation inputs (Polyak and Asmerom, 2005; Asmerom et al., 2007; Menking, 2015), and coupled ocean-atmosphere phenomena such as the El Niño Southern Oscillation and North American Monsoon (Menking and Anderson, 2003; Asmerom et al., 2007; Ballenger et al., 2011). In addition, extremes of topographic relief lead to strong precipitation gradients, highly variable evapotranspiration rates, and spatial differences in the penetration of seasonal air masses (Steenburgh et al., 2013).

Given the myriad factors that shape SW USA climate, disagreements exist between paleoclimatic records, due both to differing sensitivities of proxies and to climatic variations among geographic sub-regions. Ballenger et al. (2011), for example, reviewed a wide range of proxy evidence (speleothems, pluvial lake shorelines, pollen, packrat middens, alluvial sediments, wetland black mats, and distributions of archeological materials) from the SW USA that demonstrated inconsistent climatic and hydrologic responses to the Younger Dryas (YD) event. While the most continuous and best-dated records appear to show a transition from a warm and dry Bølling/Allerød (B/A) to a cool and wet YD, a number of records show increasingly xeric conditions throughout the YD (Ballenger et al., 2011). One such record is a speleothem (Cave Without a Name) from central Texas that led Feng et al. (2014) to suggest that errors in age control might be responsible for regional discrepancies in the timing of wet and dry intervals. Noting that their interpretation of a wet B/A followed by a dry YD conflicts with evidence from lacustrine sediments in the Estancia basin of central New Mexico that indicates a YD highstand, Feng et al. (2014) proposed that uncertainties in the radiocarbon dates used to construct the Estancia lake level chronology may have led Anderson et al. (2002) to an incorrect age assignment for this final highstand of the lake.

* Corresponding author.
E-mail address: kimenking@vassar.edu (K.M. Menking).

https://doi.org/10.1016/j.quascirev.2018.09.030
0277-3791/© 2018 Elsevier Ltd. All rights reserved.

Here we report on new U–Th dates that both supplement and strengthen the existing lake level chronology of Pleistocene Lake Estancia and allow us to extend the record of hydrologic variation backward in time to ~69 ka through analysis of a previously unreported sediment core. The dates were measured in gypsum sands and represent a tool in geochronology that may be of widespread utility in other closed basin lake systems. Furthermore, the extended record shows strong similarities to isotopic records from Fort Stanton cave in south-central New Mexico (Asmerom et al., 2010, 2017), Cave of the Bells in southern Arizona (Wagner et al., 2010), and Greenland ice cores (Rasmussen et al., 2014; Seierstad et al., 2014). The highly sensitive response of Pleistocene Lake Estancia to climatic changes resulted from a basin hydrology that provided a continuous supply of groundwater to the lake throughout the period of record. While other Pleistocene lake sediment archives were lost to deflation (e.g. Lake Otero in the Tularosa Basin of New Mexico; Allen et al., 2009) or to hydrologic changes that resulted in a lack of deposition (e.g. Lake Bonneville in Utah; Oviatt et al., 1999), the Estancia Basin was able to record intervals of wetter climate and drought at decadal to millennial scale resolution (Allen and Anderson, 2000; Menking, 2015). The record presented here is thus among the most highly resolved and complete non-speleothem records available in the SW USA throughout marine isotope stages 2, 3, and 4.

2. Study setting

Estancia basin and its late Pleistocene lake (Fig. 1) are described extensively in Allen and Anderson (2000), Anderson et al. (2002), and Menking and Anderson (2003). The 5000 km^2 basin is bordered on its western edge by Precambrian and Paleozoic sedimentary rocks of the Manzano Mountains, which form the highest part of the drainage divide and intercept the majority of precipitation. Dissolution of limestone and gypsum has created a karstic aquifer system that conveys groundwater recharge in the Manzanos to discharge points on the basin floor. In addition to groundwater, a centripetal pattern of streams fed Lake Estancia at various times during the Pleistocene, with most of the runoff also originating in the Manzanos. At present, precipitation is strongly seasonal (Fig. 1a), produced by Pacific cyclones traveling inland with zonal winds in winter (Bryson and Hare, 1974) and by North American Monsoon moisture drawn largely from the Gulf of Mexico in summer (Hales, 1974). Isotopic measurements indicate that groundwater recharge is dominated by winter precipitation, with summer rains contributing negligibly (Menking and Anderson, 2003).

Radiocarbon-dated shoreline and basin-center deposits show that Pleistocene Lake Estancia fluctuated in size between 400 and 1100 km^2 and ~5 and 45 m water depth at least nine times from 28.8 to 13.9 ka (24–12 ^{14}C kyrs B.P., Allen and Anderson, 2000). Two highstands pre-date the LGM, five occurred during the LGM, and two post-date the LGM (16.9 and 14.6 ka; reported as 13.8 and 12.5 ^{14}C kyrs B.P.). The post-LGM highstands occurred after a protracted interval (18.1–17 ka) of drawdown popularized by Broecker et al. (2009) as the “Big Dry”, during which lake level fell to only a few meters depth (Allen and Anderson, 2000). After the post-LGM highstands, desiccation of the lake at ~14 ka resulted in the precipitation of an ~50-cm thick layer of mostly homogeneous gypsum and magnesite on the basin floor that was sculpted by winds into a series of dune forms (Allen and Anderson, 2000). A final highstand reworked the dunes on the eastern edge of the lake into a series of beach ridges, and radiocarbon evidence bounding these features strongly supports a Younger Dryas age (Anderson et al., 2002).

Following the Younger Dryas, the lake again desiccated, and a two-stage drought during the middle Holocene dropped the level of the water table below the basin floor (Menking and Anderson, 2003). Subsequent wind excavation of more than 80 deflation basins (Fig. 1b and c) exposed part of the late Pleistocene lacustrine sequence, revealing stratigraphic changes that were correlated to shorelines through a combination of ostracode biostratigraphy and radiocarbon dating (Allen and Anderson, 2000). Basin center deposits associated with late Pleistocene highstands consist of bioturbated clays rich in calcium carbonate and ostracodes with low salinity tolerances. Lowstand sediments consist of laminated gypsum sands and algal mats and contain ostracodes with salinity tolerances >200,000 ppm. Transitions between lowstand and highstand sediment sequences are generally abrupt, and this, combined with radiocarbon dates, suggests that shifts between lowstand and highstand lake levels occurred in a matter of decades (Allen and Anderson, 2000). Spectral analysis of mineralogical time series reveals decadal to millennial cycles consistent with solar forcing during the Last Glacial Maximum (LGM; Menking, 2015).

Since the end of the middle Holocene drought, wetter conditions have eroded lunettes created by excavation of the deflation basins, returning some of the excavated material to each blowout where it creates a playa fill deposit that overlies the wind-cut surface (Fig. 1c). The depth of excavation and thickness of the overlying fill varies from blowout to blowout, but the same general stratigraphic units are found in the walls of each of the depressions, allowing correlation of the late Pleistocene lake sediments throughout the basin.

3. Methods

Previous work conducted in the Estancia Basin (Allen and Anderson, 1993, 2000; Anderson et al., 2002; Menking and Anderson, 2003) focused on the stratigraphic record exposed in the walls of the deflation basins, in dune and shoreline deposits, in stream delta sediments, and in playa fill deposits and covered the time interval ~28.8 ka to the present. To extend the record backward in time, we obtained a 2.8-m-long sediment core from beneath the floor of the Laguna del Perro playa (LDP), the blowout with the greatest depth of wind excavation into the Pleistocene lake sequence (Fig. 1). The core measures 5 cm in diameter and was taken in five drives using a percussion coring rig. After extraction, the core was wrapped in plastic wrap and placed in PVC pipe for transport to the University of New Mexico. In the lab, the core was split in half lengthwise, photographed, and described prior to sampling for U–Th dating.

A hydrologic balance index (HBI) was devised based on the physical appearance and mineralogical composition of core sediments. Thickly bedded (>1 cm) bioturbated marls associated with lake highstands were assigned an end-member HBI value of 5 whereas thinly laminated (<1 mm) gypsum sands and algal mats associated with lowstands or playa deposition were assigned an end-member value of 1. Full descriptions of the different hydrologic balance index values along with accompanying photographs can be found in the appendix for this paper (see Fig. A1). After definition, HBI values were determined at 1-cm resolution throughout the entire length of the core (Fig. A2 in the appendix shows examples).

To facilitate comparison of the HBI values in the core to previous work on the overlying late Pleistocene lake sequence, HBI values were also determined on sediments found in the walls of two deflation basins with vertically overlapping exposures. Outcrop sediments exposed in the wall of the E-19 blowout (Fig. 1b) span 7.8 m from the base of the gypsum and magnesite desiccation layer, called the B-zone by Bachhuber (1971) and used here as the 0-m datum for the combined core and outcrop HBI time series, downward into a unit named the F-zone that was deposited in conditions of shallow lake levels that prevailed prior to LGM expansion of Lake

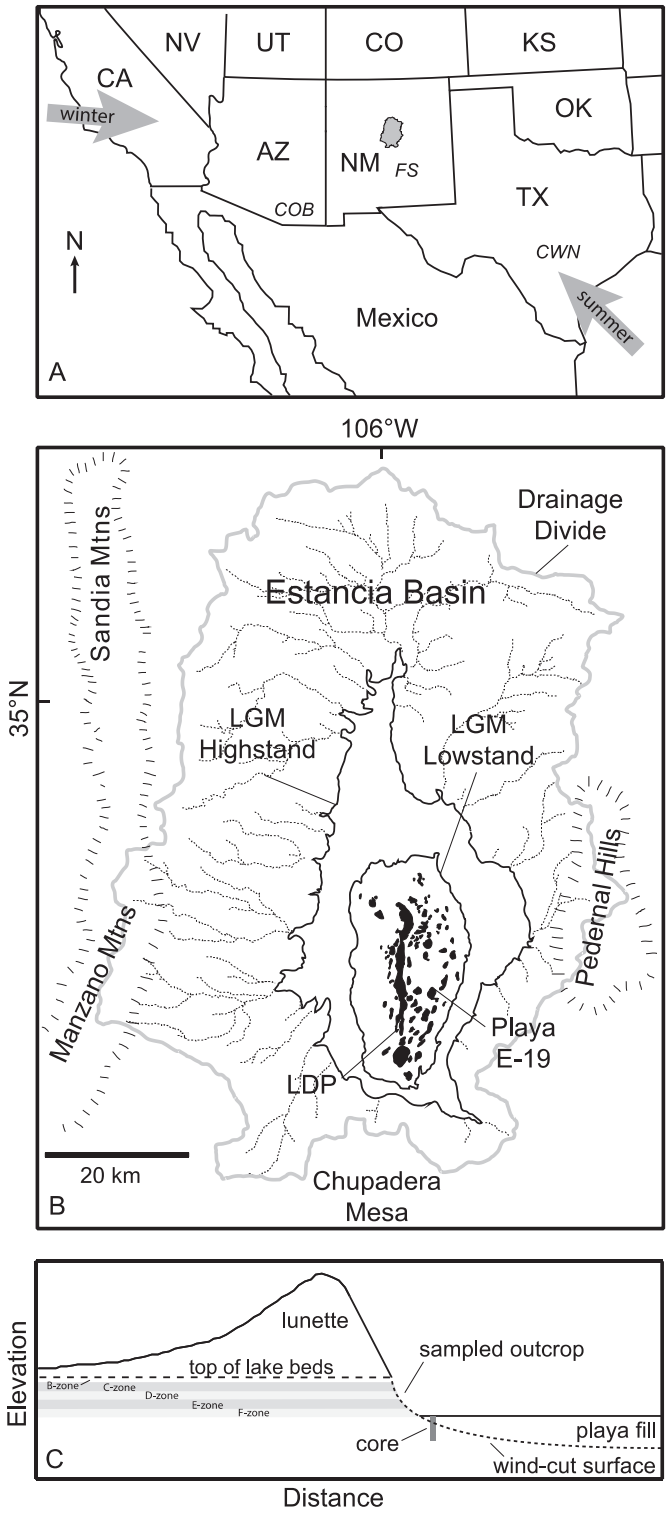


Fig. 1. A) Location of the Estancia Basin (gray shaded region) in central New Mexico. FS, COB, and CWN mark the locations of the Fort Stanton, Cave of the Bells, and Cave Without a Name speleothem records. Gray arrows show the source regions for modern precipitation. B) Inset map of the Estancia Basin showing the positions of Last Glacial Maximum (LGM) highstand and lowstand shorelines, physiographic features that make up the drainage divide, and the centripetal pattern of streams that fed the highstand stages of the lake. Black shaded regions enclosed by the LGM lowstand shoreline are the >80 deflation playas excavated into the lake floor sediments during a two-stage drought in the middle Holocene. Black lines point to the locations where outcrops were trenched for this study in the E-19 and Laguna del Perro (LDP) playas and where the LDP core was taken. C) Schematic diagram of the stratigraphic relationships between the sampled outcrops and the sediment core. Stratigraphic zones after Bachhuber (1971). See Fig. 2 for more information.

Estancia (Fig. 2). Outcrop sediments were trenched and trench walls carefully scraped clean to reveal stratigraphic changes that were then photographed, with a tape measure used to provide scale. HBI values were assigned at 2.5-cm intervals.

The boundary between the F-zone and overlying LGM sediments (called the E-zone by Bachhuber, 1971) was re-located in the walls of the Laguna del Perro (LDP) playa immediately adjacent to the site of the core (Fig. 1) using a distinctive pelecypod-rich marker horizon (*Pisidium sp.*, Allen and Anderson, 2000, Fig. 2) and the underlying F-zone sediments similarly trenched and photographed to the base of the outcrop (7.16–9.69 m below the B-zone datum). HBI values were assigned at a 1-cm interval. There is an ~30 cm gap in the HBI record between the base of the outcrop in the LDP deflation basin wall and the top of the Pleistocene sequence in the sediment core (Fig. 2). This gap is associated with the late Holocene infilling of the basin by eroded lunette materials that rest atop the middle Holocene deflation surface to create a playa fill deposit (Fig. 1c).

Chronological control for the HBI series was acquired from a combination of 22 previously reported ostracode radiocarbon dates (Allen and Anderson, 2000; see Table A.1 in the appendix) and eight new U–Th dates measured on gypsum sands. Twenty of the radiocarbon dates extend along the vertical length of the E-19 deflation basin outcrop. The other two lie within the LDP F-zone exposure at stratigraphic elevations lower than the lowermost F-zone date in E-19 (Fig. 2). Radiocarbon dates were converted to calendar ages using the Calib 7.10 software with the IntCal13 calibration curve (Stuiver et al., 2018).

The U–Th dates were acquired by collecting pieces of gypsum-rich sand layers from outcrop exposures and the core (Fig. A3 in the appendix shows a photograph of typical gypsum sand grains). One sample was taken from the base of the gypsum-magnesite B-zone layer, two were taken in the E-zone layer for calibration purposes discussed below, three were taken from the F-zone layer in the wall of the LDP playa sampling site and are interstratified with the two previously reported ostracode radiocarbon dates, and four were taken from the LDP sediment core. All surfaces of the gypsum sand samples were shaved until clean flat surfaces were available for sampling. For most intervals, three to six ~100 mg sub-samples of gypsum sand were shaved along the sand layers. Gypsum and magnesite were separated using a magnetic mineral separator for the B-zone sample, except for samples B-1 through B-4, for which magnesite was separated by dissolving the gypsum in 0.5N HNO_3 acid. The gypsum sand sub-samples were dissolved in 1N HNO_3 for 48 h, treated with an in-house ^{236}U–^{233}U–^{229}Th mixed spike and agitated in a sonic bath for 1 h. U and Th were removed from this solution by adding Fe chloride solution and co-precipitating the Fe, U, and Th using an ammonium solution. The insoluble sediment containing U and Th was cleaned and separated from Ca, Mg, S, and other elements in the solute by centrifugation. The sediment was then dissolved in 15N nitric acid and dried, followed by dissolution in 7N HNO_3 for loading into resin columns. The magnesite separates were dissolved in 15N HNO_3, spiked, and loaded into resin columns. U and Th were cleaned and separated in anion resin columns following the procedures of Asmerom et al. (2010).

The separates after the column chemistry were further dissolved in 3% HNO_3 and run on a Micromass Sector 54 thermal-ionization mass spectrometer (TIMS) and Neptune plus multi-collector inductively coupled plasma mass spectrometer (MC-ICPMS) at the University of New Mexico Radiogenic Isotope Laboratory using a CETAC Aridus II desolvating nebulizer intake that enhances the signal on the MC-ICPMS. All runs on the MC-ICPMS were static measurements, and U and Th were run separately. All measurements were made in Faraday cups except for ^{230}Th and

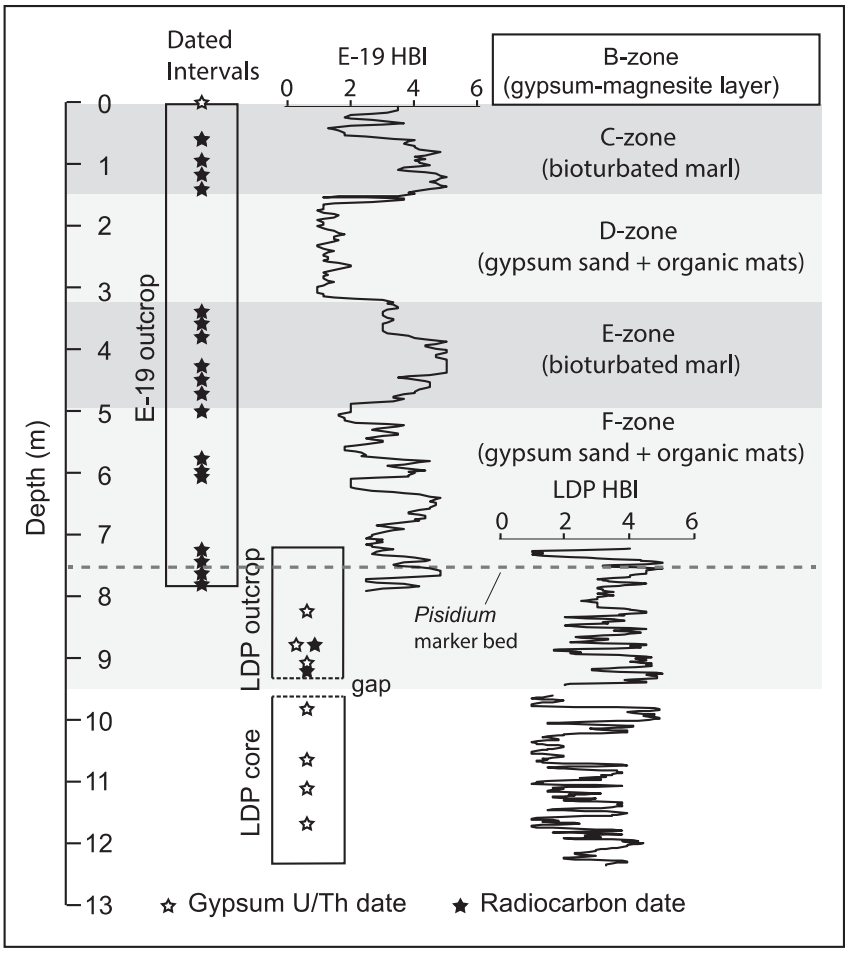


Fig. 2. Stratigraphic relationships for the HBI series. LDP = Laguna del Perro playa, E-19 = E-19 playa (see Fig. 1 for locations). Gray shading shows outcrop unit boundaries first described by Bachhuber (1971) and later used by Allen and Anderson (2000). Sediments exposed in the E-19 section showed less variable stratigraphy than those in the underlying LDP outcrop and LDP core sequences and were therefore sampled at a coarser resolution (2.5 cm sample spacing for E-19 vs. 1 cm spacing for LDP) for the HBI analysis. An HBI series constructed on an outcrop in another deflation basin (E-20) 4 km to the northwest of E-19 (unpublished data) showed nearly identical variations to those in E-19, indicating that our qualitative index is a robust measure of hydrologic variability.

^{234}U, which were measured with a secondary electron multiplier. Gain values between the secondary electron multiplier and the Faraday cups for each sub-sample run were determined using an NBL-112A uranium standard and an in-house ^{230}Th standard. Total average procedural blanks are 0.05 fg ^{230}Th, 5 pg ^{232}Th, and 20 pg ^{238}U.

Ages were calculated using decay constant values reported in Cheng et al. (2013) and an initial ^{230}Th/^{232}Th atomic ratio of 4.4 (±4.4) $\times 10^{-6}$ (ppm). The B-zone gypsum-magnesite layer age determination is highly sensitive to the initial ^{230}Th/^{232}Th value used for age correction, and for that reason, the initial ^{230}Th/^{232}Th value was measured. This value can be measured by using the isochron method, or by adjusting the initial ^{230}Th/^{232}Th value to a known age. For example, a ^{232}Th/^{238}U–^{230}Th/^{238}U–^{234}U/^{238}U 3-dimensional isochron of sample F-3 produced an initial ^{230}Th/^{232}Th value of 2.3 ± 6.8 ppm. In our case, isochrons were not calculable, or precise enough. Instead, the initial ^{230}Th/^{232}Th value was measured using four sub-samples of two gypsum layers in the well-dated E-zone (see Fig. A4 in the appendix). Three analyses of sample E-1 (3.5 m below the B-zone 0 m datum) and one analysis of E-2 (4.1 m below the datum) have measured sample (not initial) ^{230}Th/^{232}Th values of 6–7 ppm, and like the isochron value, show that the initial ^{230}Th/^{232}Th value is low. Adjusting the U–Th age of each of these four subsamples to the calculated calendar age chronology from seven ^{14}C dates within the 1.7 m-thick E-zone yielded what we interpret to be more accurate initial ^{230}Th/^{232}Th values of 3.59, 4.46, 4.99, and 4.67 ppm (avg. = 4.43 ppm; Table A.2), justifying the use of the value of 4.4 ppm derived from the bulk earth ^{232}Th/^{238}U value (Cheng et al., 2013) used to correct our U–Th dates.

Because gypsum is more soluble than calcite, ages of multiple sub-samples (n = 3 to 6) from each sample were measured to test repeatability, and those values were weight-averaged using Isoplot (Ludwig, 2000) to obtain an average age having an absolute 2σ error dependent on repeatability. Our age for the gypsum-magnesite layer (Bachhuber's B-zone; 0-m datum for the HBI series) is based on the weighted average of 16 dates on 11 magnesite and gypsum separates. Each sub-sample had high concentrations of detrital thorium as would be expected in lake sediments, so multiple analyses of different sub-sample separate types and treatment methods were performed, as listed in Table A.2. Once measured, the new U–Th and previously determined ^{14}C dates were input into the COPRA age modeling software (Breitenbach et al., 2012) to create an age/depth model for the combined HBI sequence.

4. Results

Uranium and thorium concentrations, activity ratios, and corrected ages for all replicate analyses on each of the eight gypsum samples analyzed are reported in Table A.2 in the appendix. Weighted-average ages (see footnote on Table A.2 for more information) from these results are in stratigraphic order, and the combined age model can be found in Fig. 3. The two radiocarbon dates located within the LDP F-zone outcrop (gray shaded region between 7.9 and 9.6 m depth on the figure) appear to be too young by 1500–3500 years in the context of the U–Th ages of the gypsum samples, creating a non-tractable age reversal for COPRA (Breitenbach et al., 2012). We therefore excluded them in the creation of the age model. Still, the fairly close agreement of these dates with the adjacent gypsum dates lends credence to the U–Th values, as does the shape of the combined age model, which resembles a typical concave-up compaction curve.

The U–Th age of the gypsum-magnesite desiccation layer (B-zone) that serves as the 0-m datum for the HBI series is 13,916 ± 850 years (a statistically weighted average age from 16 analyses, see Fig. A5 in the appendix) and is also in stratigraphic order with the radiocarbon and other U–Th dates. The HBI time series constructed by combining the age-modeled values from the E-19 and LDP outcrops and LDP core is shown in Fig. 4 (data in Table A.3 in the appendix) along with isotopic records from three SW USA speleothems and the GISP 2 ice core from Greenland. HBI values fluctuate widely on centennial to millennial timescales, with pronounced variability between ~55 and 69 ka, an interval characterized by oscillations between shallow lake and playa conditions based on sedimentological evidence (Bachhuber, 1971). Particularly low values of HBI can be found from 57 to 52, 45-43, 18-17 (the "Big Dry" of Broecker et al., 2009), and 14.5 to 14 ka, whereas sustained high values occur during the LGM and from 17 to 14.5 ka.

5. Discussion

5.1. U/Th dates on gypsum sands

The gypsum layers newly dated in this study are interpreted as an accumulation of gypsum sand grains that were originally precipitated out of groundwater discharging to mudflats surrounding the contracted lake during lowstands and then washed or blown into the lake center (Allen and Anderson, 2000). Uranium was incorporated into the gypsum as a substitution for calcium during mineral formation. While gypsum is exceedingly more soluble in water than calcite or magnesite, the brininess of the lake water trapped in the gypsum layers, as evidenced by accompanying ostracodes with very high salinity tolerances (Allen and Anderson, 2000), in combination with the layers being "sealed" between clay-rich sediments deposited during higher lake levels, resulted in pristine preservation of the gypsum that facilitated the dating. The U–Th ages of the sub-samples of each layer showed reproducibility beyond expectations for the pure gypsum sands located in the F-zone outcrop at LDP and in the underlying core (see Table A.2), thus U–Th dating of well-preserved gypsum sands that crystallized coeval with sedimentation could be a potentially useful technique in other lake basins.

Even though the individual B-zone ages seemed to differ significantly, when considering their absolute 2σ errors, they produced a weighted average age that we interpret as accurate. Here we use the technique to confirm the timing of a final highstand of Lake Estancia and to extend the Estancia basin chronology further

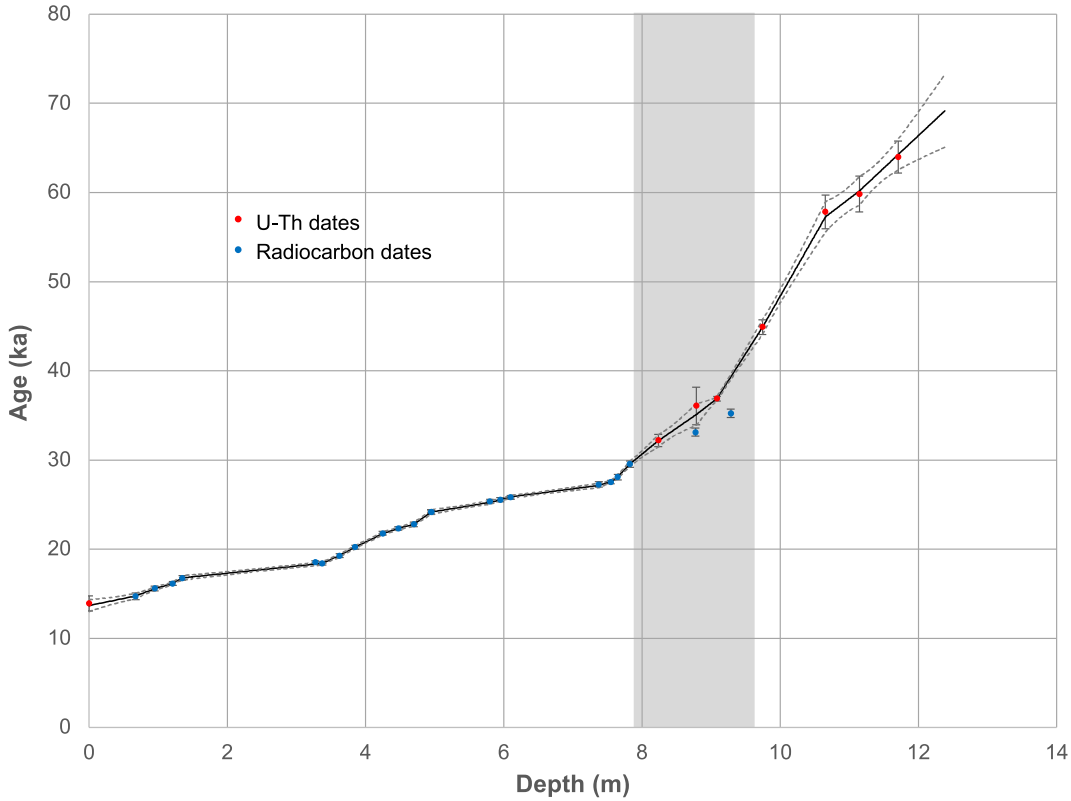


Fig. 3. COPRA age model for the combined outcrop and core HBI series. The two radiocarbon dates within the gray shaded region (LDP F-zone outcrop dates) are too young in the context of the U-Th dates and were excluded from the age model.

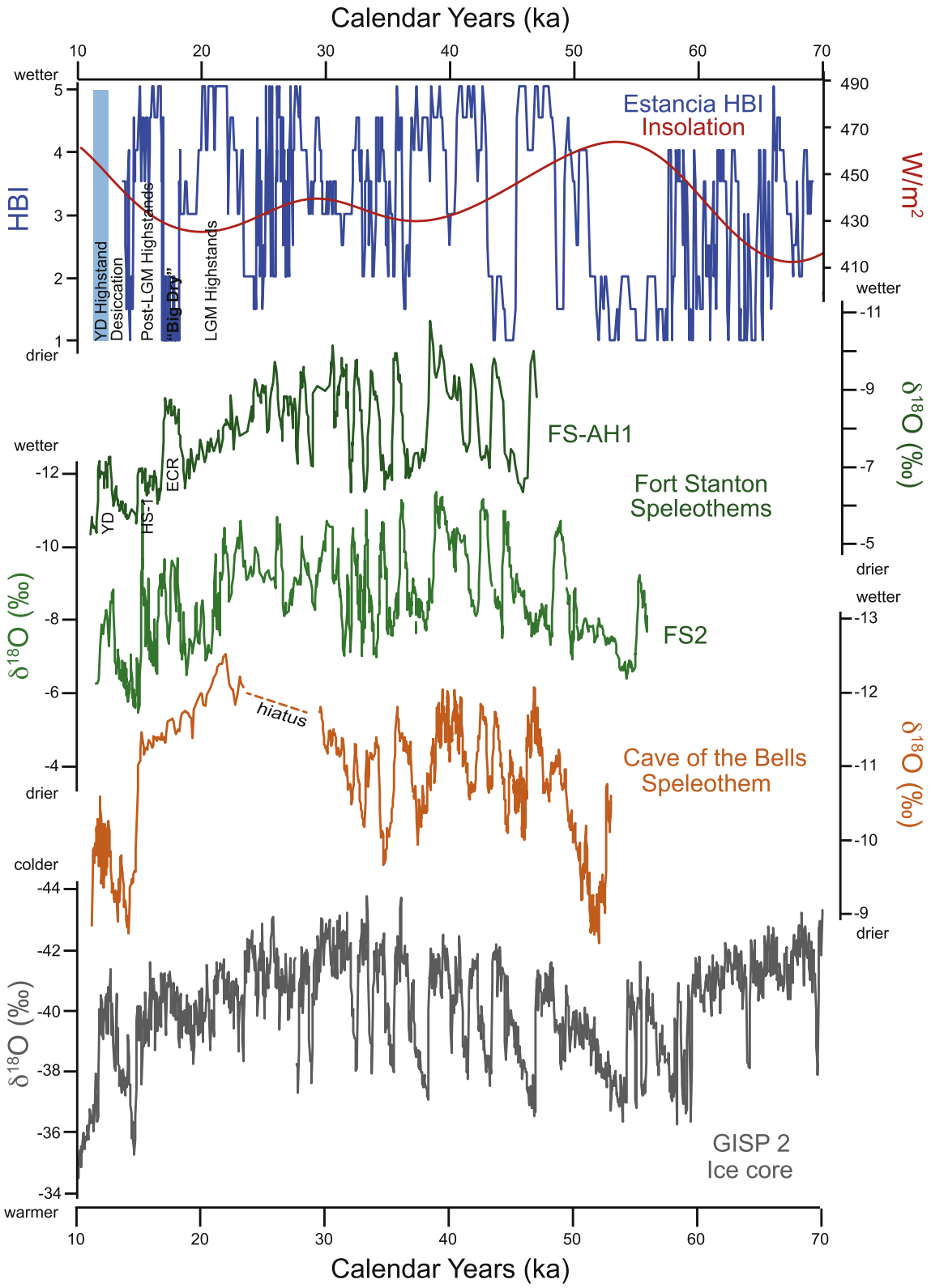


Fig. 4. Comparison of the Estancia Basin HBI record to speleothem records from southern New Mexico (FS2 and FS-AH1 from Fort Stanton Cave; Asmerom et al., 2010, 2017) and Arizona (Cave of the Bells; Wagner et al., 2010) as well as the GISP 2 ice core record (Rasmussen et al., 2014). Also shown is the record of northern hemisphere insolation (65°N) during the month of July (Huybers and Eisenman, 2006). YD refers to Younger Dryas, HS-1 to Heinrich Stadial 1, LGM to Last Glacial Maximum, and ECR to the Extrapolar Climate Reversal of Asmerom et al. (2017). In general, wetter conditions in the Estancia Basin and speleothem records correspond to colder conditions in the GISP 2 ice core record, whereas drier conditions correspond to warmer conditions.

back in time to a period prior to the major rise in lake level when the basin floor oscillated between shallow water conditions and more playa-like states.

5.2. Conditions during the Bølling/Allerød and Younger Dryas

The U–Th ages of subsamples of the gypsum-magnesite B-zone desiccation layer show a bit higher range of variation than those of the F-zone gypsum sands, but yield a weighted average value of 13,916 ± 850 years (n = 16). Allen and Anderson (2000) presented radiocarbon evidence bracketing the age of the B-zone layer and a subsequent lake highstand that reworked that layer into a series of beach ridges to between ~13,860 yr B.P. (Calib 7.10 IntCal13 calibration from reported date of 12,000 ^{14}C yr B.P.) and ~11,000 yr B.P. (Calib 7.10 IntCal13 calibration from reported date of 9650 ^{14}C yr B.P.). The new U–Th age thus supports the previously reported interpretation (Allen and Anderson, 2000; Anderson et al., 2002) that the Bølling-Allerød interstadial was dry in the Estancia Basin, followed by a wet Younger Dryas. Core and shoreline evidence from Lakes Lahontan and Bonneville similarly show low levels during the Bølling-Allerød and higher levels during the Younger Dryas (Benson et al., 2011, 2013; Oviatt, 2015, identified a regression of Lake Bonneville to the modern Great Salt Lake level by 13 ka). Likewise, Asmerom et al. (2010) interpreted isotopically depleted δ^{18}O values from a speleothem in Fort Stanton Cave to reflect a wet Younger Dryas after a drier Bølling-Allerød, and other southern New Mexico speleothems also corroborate these findings (Polyak et al., 2004, 2012). For example, Polyak et al. (2012) clearly show δ^{13}C and δ^{234}U evidence for drying of the southwestern United States starting at 14.6 ka, supported by shelfstone speleothem dates that indicate the drying of pool basins in the Big Room of Carlsbad Caverns soon after 14 ka. The ~14 ka B-zone gypsum-magnesite layer in the Estancia Basin is thus an exceptionally good marker for termination of the wet conditions that produced Pleistocene lake highstands in the southwestern United States.

Further support for a moist Younger Dryas in the Estancia Basin comes from wet meadow sediments found in a presently dry arroyo just outside the southwestern corner of the Estancia Basin. Hall et al. (2012) reported radiocarbon dates on organic material and charcoal fragments in these sediments that indicate wet conditions starting about 500 years into the YD and lasting 400 years beyond its termination in the early Holocene (10,400 to 9700 ^{14}C yrs B.P., corresponding to 12,270 to 11,130 yrs B.P.). Based on a speleothem record from southern New Mexico's Guadalupe Mountains, Polyak et al. (2004) also interpreted this wet period to have started in the YD and to have lasted beyond the YD. Furthermore, black mat sediments deposited at the Murray Springs Clovis culture site in southeastern Arizona between 12,700 and 11,100 yrs B.P. (10,700 and 9700 ^{14}C yrs B.P.) have been interpreted to reflect wetter conditions (Haynes et al., 2010). Indeed, black mat sites throughout the western United States show evidence of wet conditions between 12,800 and 11,200 yrs B.P. (10,900 and 9800 ^{14}C yrs B.P.; Haynes, 2008). The end of this wet interval, while not exactly coincident with the YD, closely matches the timing of the end of the highstand that occurred between 13,860 and 11,000 yrs B.P. for Lake Estancia reported by Allen and Anderson (2000), suggesting that the response of the SW USA to YD cooling and associated wetter conditions somewhat lags that of the Atlantic Basin.

5.3. Conditions during the "Big Dry" and "Mystery Interval"

The pronounced low value in the Estancia HBI record from 18 to 17 ka marks an unexpected distinct and significant lake lowstand after the LGM, dubbed the "Big Dry" (Broecker et al., 2009). The carefully established radiocarbon chronology of the Estancia Basin made it possible for Broecker et al. (2009) to show that this lowstand was part of a global climate "Mystery Interval" in which several paleoclimatic records that had previously fluctuated in concert with oxygen isotopic variations in the Greenland ice sheet instead showed other behaviors. Our comparison of the Estancia HBI with the nearby Fort Stanton stalagmite FS-AH1 oxygen isotope record (Fig. 5) shows a remarkable match of the "Big Dry" lowstand with the Extrapolar Climate Reversal (ECR) of Asmerom et al. (2017) from 18.6 to 17 ka. The FS-AH1 record has an untuned correlation of R = 0.63 with the Greenland Ice Core (GIC) oxygen isotope record of Rasmussen et al. (2014), and the stadial and interstadial isotope excursions of FS-AH1 and the GIC generally match well in the two records, suggesting that colder conditions in Greenland were associated with a dominantly winter-like circulation pattern in the SW USA in which deflections in the polar jet stream increased Pacific-sourced precipitation. The two records are highly correlated except for the distinct low-value isotope excursion in FS-AH1 that defines the ECR, suggested by Asmerom et al. (2017) to be linked to increased upwelling of Southern Ocean water in the subtropics and associated extrapolar hydroclimatic effects. The existence of the Estancia "Big Dry" lowstand during the ECR suggests that effective moisture was lowered at Fort Stanton cave even as the oxygen isotope excursion in FS-AH1 indicates that Pacific or winter-like moisture was the dominant source of precipitation, which adds evidence to the interpretation of a non-North Atlantic origin for this event. Increased upwelling of Southern Ocean water in the subtropics may have resulted in a southward shift of the Intertropical Convergence Zone in the tropical Pacific and a decline in sea surface temperatures in the northeastern Pacific, leading to the cold but drier conditions. The Estancia HBI evidence for two lake highstands immediately following the "Big Dry" are coeval with Heinrich Stadial-1 (HS-1 in Fig. 5) in the FS-AH1 record, showing that cooler, wetter climate prevailed until roughly 14 ka, when Pleistocene Lake Estancia dried up during the B/A. As such, the coupling between Greenland ice sheet temperature and effective wetness in the Southwest appears to have been reestablished immediately after the "Big Dry"/ECR.

5.4. Climate conditions from 19 to 69 ka

Additional wet-dry oscillations throughout the Estancia HBI record are broadly similar in timing and duration to events in the Fort Stanton and Cave of the Bells speleothems as well as to temperature variations in the GISP 2 ice core. Given constraints of the age model, we are hesitant to draw too many direct comparisons between Estancia Basin and the other records, though it is interesting to note that prominent lows in HBI value from ~57 to 51 ka and from ~45 to 43 ka in the Estancia record are similar in timing to seemingly dry intervals in Fort Stanton and Cave of the Bells as well as warmer intervals in the GISP 2 record (Fig. 4). Relatedly, all three speleothem records show wetter conditions from ~41 to 38 ka, a time during which the HBI in Estancia shows values consistent with higher water levels and the GISP 2 record indicates colder conditions.

The period of lake lowstands from 57 to 51 ka marks the time when the Cave of the Bells and Fort Stanton Cave FS-2 stalagmites began growing. The lowstands and isotopically enriched speleothem values are coeval with a northern hemisphere summer insolation peak (July 21, 65 N) at ~54 ka, consistent with an interpretation of climate too dry to form lake highstands (Fig. 4). It was after this insolation peak that conditions apparently became more suitable for

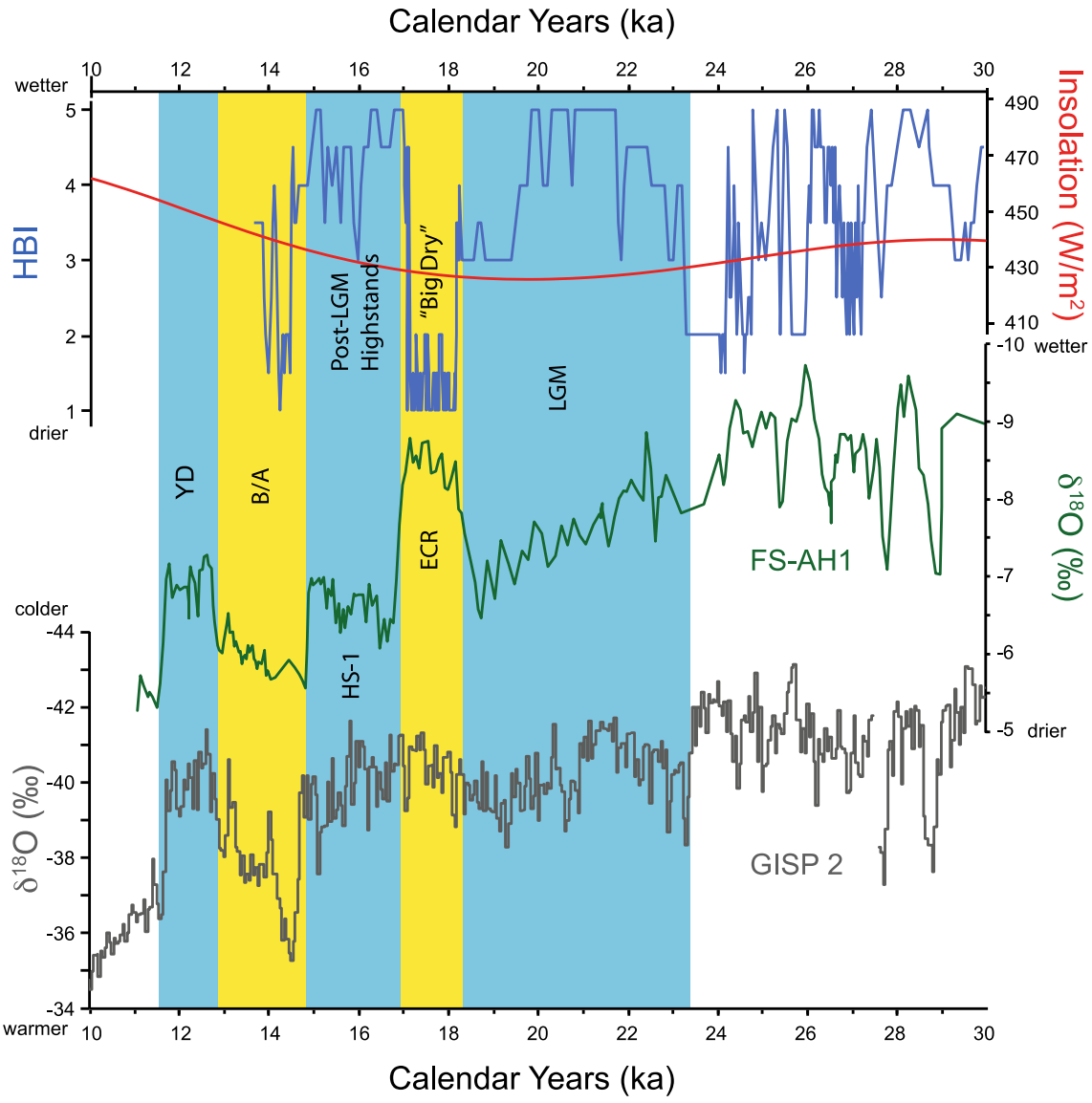


Fig. 5. Closer view of the Estancia HBI, Fort Stanton AH-1, GISP 2, and insolation records for the interval 10-30 ka. Blue shaded bars reflect wetter conditions in the Estancia Basin and yellow shaded bars show drier intervals. Note the close temporal correspondence between the ECR of Asmerom et al. (2017) and the "Big Dry" in the Estancia record. Low values of insolation at this time do not appear to explain the "Big Dry.". (For interpretation of the references to colour in this figure legend, the reader is referred to the Web version of this article.)

both higher lake levels and growth of stalagmites in Fort Stanton Cave. It is interesting to note that the Estancia Basin and Fort Stanton speleothem records show that the onset of the Holocene also was too dry for deposition of lacustrine sediments or stalagmites, a time of similarly high summer insolation values to those that prevailed at 54 ka. Lower insolation values may have been partly responsible for the somewhat wetter conditions that led to the oscillating HBI values between 69 and 57 ka in the Estancia basin.

5.5. *Response to wetter Bølling-Allerød, drier Younger Dryas interpretation*

While the Estancia Basin radiocarbon chronology has created one of the most robust records of climatic change for the southwestern United States, an alternative interpretation of a wetter B/A and drier YD was introduced by Feng et al. (2014), based on a stalagmite study from Cave Without a Name in central Texas, east of the region generally considered to be the SW USA. These workers questioned the accuracy of the Estancia Basin ^{14}C chronology, suggesting that the second post-LGM highstand took place during the B/A, and that desiccation of Lake Estancia, represented by the B-zone gypsum-magnesite layer, took place during the YD. Here, we have shown that the Estancia U–Th and radiocarbon chronologies complement one another, and with consideration of the other important studies on this subject mentioned above, we suggest that the Cave Without a Name study site is not representative of the SW USA.

Another line of evidence used by Feng et al. (2014) to support their interpretation of a wet B/A and dry YD was faster growth rates in the Fort Stanton stalagmite FS-2 during the B/A, which they suggested were evidence for wetter climate as was demonstrated by Polyak et al. (2004) for speleothems from the Guadalupe Mountains of southern New Mexico. This interpretation is too broadly applied, however. Stalagmites FS-2 and FS-AH1 grew

in an ~100% relative humidity cave environment, which leads to slow precipitation and is far different from the evaporative conditions found in the caves of the Guadalupe Mountains. Thus, a more likely interpretation for the higher growth rate of the FS-2 speleothem during the B/A is that warmer, drier conditions led to faster rates of calcite precipitation. Such a relationship has been reported for stalagmite growth in caves of NW Scotland (Baker et al., 2015).

6. Conclusions

Our study has produced a record of substantial hydrological change during deglaciation in the SW USA, demonstrating that the B/A was a dry period. While desiccation of Lake Estancia took place during the B/A, an additional rewetting took place during and/or around the YD, consistent with a YD and early Holocene wet period proposed by Polyak et al. (2004) from stalagmites, Hall et al. (2012) from wet meadow deposits, and Haynes (2008) from black mats throughout the western United States. The pronounced "Big Dry" lowstand (17-18 ka) supports the interpretation of Asmerom et al. (2017) that an isotopic excursion in the Fort Stanton speleothem record from 17 to 18.6 ka reflects a decoupling of southwestern climate from global variations. Otherwise, the Estancia HBI series indicates quite similar climatological variability to that seen both at Fort Stanton and in Greenland, with overall wetter conditions during stadials and drier conditions during interstadials.

Acknowledgements

This work was supported by National Science Foundation grants EAR-9304360, EAR-9019134, and EAR-0326902. We thank Mike and Sue Harvey for access to the sites and Bruce Allen for his assistance in taking the sediment core and trenching the outcrops at playa E-19 and Laguna del Perro. We also thank Susan Zimmerman and two anonymous reviewers, whose thoughtful comments improved the manuscript.

Appendix

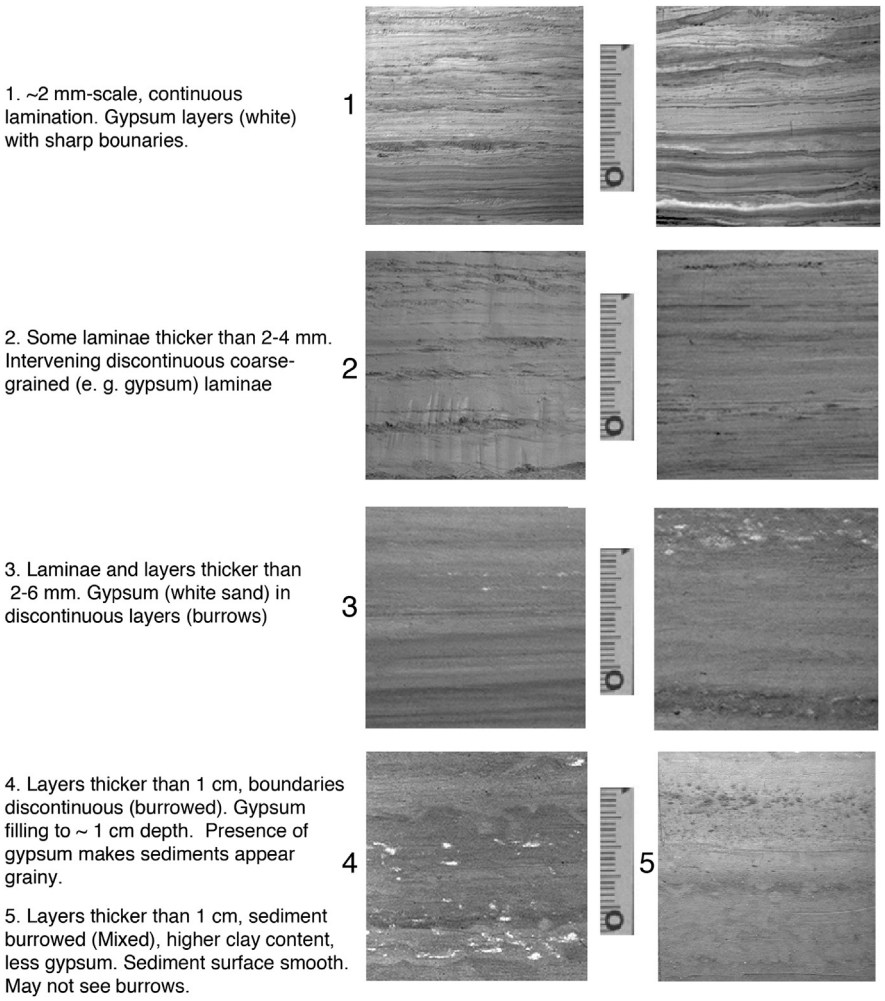


Fig. A.1. Hydrologic Balance Index (HBI) classification scheme. Scale bars between photographs are each 5 cm long.

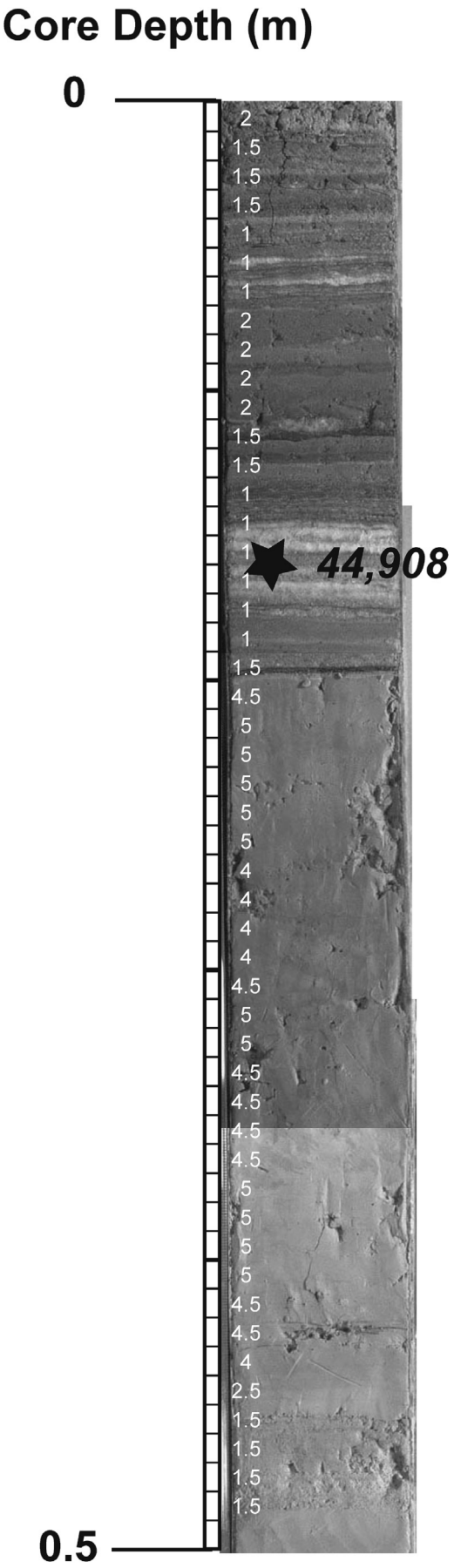


Fig. A.2. Sample photos from the Laguna del Perro (LDP) core showing HBI values (white numbers) for each centimeter of depth. Star marks the position of one of the gypsum sand intervals dated via U–Th. Color change at ~0.35 m is an artifact of the use of overlapping photographs and not stratigraphically meaningful.

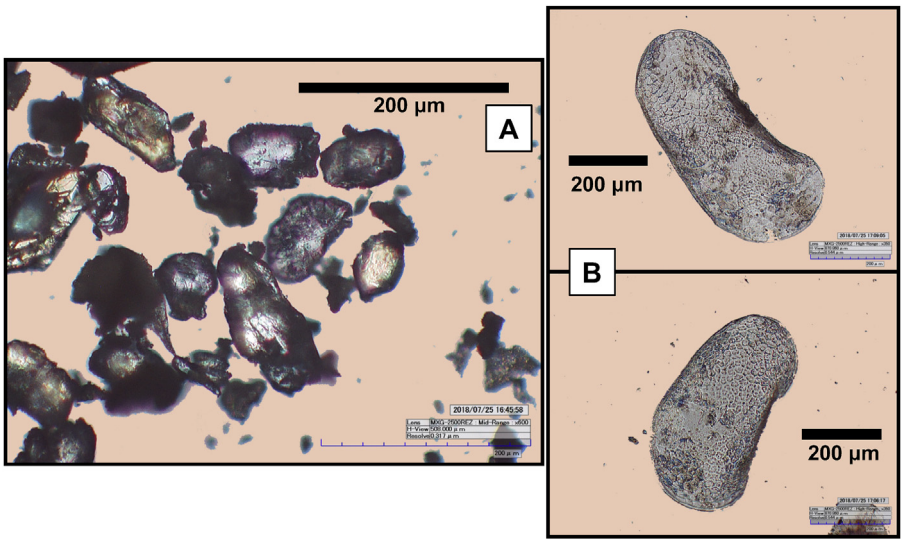


Fig. A.3. Optical digital microscope images of gypsum sand (A, layer F3) and ostracodes (B). Sand layers consist of rounded to sub-rounded crystals of gypsum as well as smaller crystal fragments. The sand grains vary in size from ~10 to 200 µm in diameter. See Allen and Anderson (2000) for detailed description and scanning electron microscope images of the sand grains. Ostracodes are moderately abundant in some gypsum sand layers. These are from layer F3.

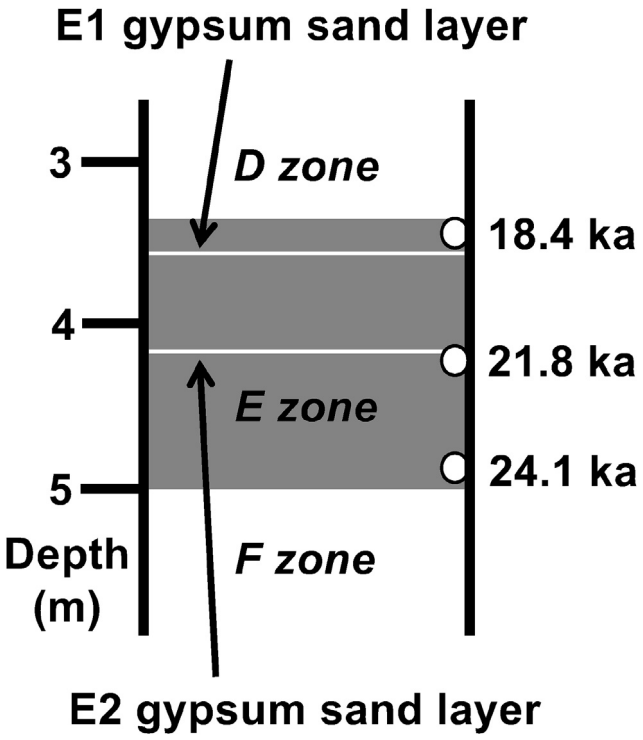


Fig. A.4. U–Th analyses of two gypsum sand layers within the well-dated E zone that were used to determine the initial $^{230}Th/^{232}Th$ value (Values are listed in Table A.2). Analyses of three subsamples of sample E1 and one subsample of sample E2 yielded a measured initial $^{230}Th/^{232}Th$ (atomic ratio) value of 4.4×10^{-6} (4.4 ppm). E1 is projected to be 18,720 yrs B.P., and E2 is projected to be 21,032 yrs B.P., based on the highly resolved ^{14}C chronology across the seven ^{14}C dates in the 1.7 m-thick E zone. Only three of the seven ^{14}C dates are shown in this figure, which was modified from Fig. 3 of Allen and Anderson (2000).

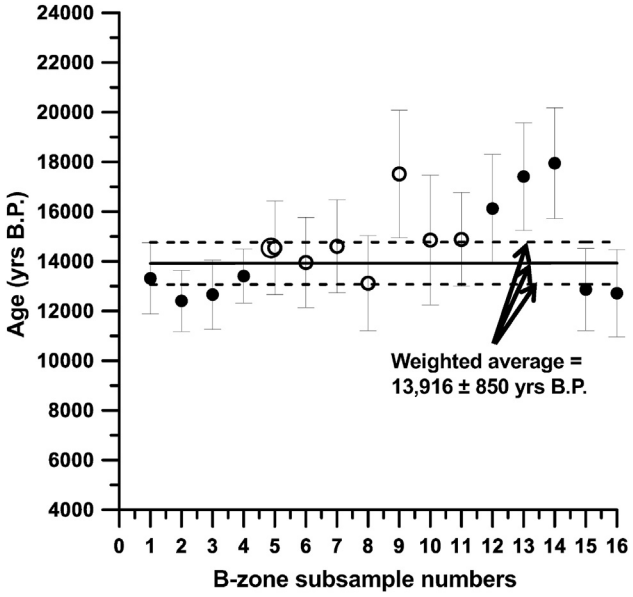


Fig. A.5. U–Th analyses of the B-zone sample at the top of the stratigraphic column. 16 U–Th ages were measured from this sample. Filled circles are measured ages and 2σ absolute errors of magnesite separates. Empty circles are ages and errors of gypsum separates. The double circle (#5) is a mixture of gypsum and magnesite. The weighted average age and 2σ error are represented by the solid and dashed lines (see Table A.2). Magnesite subsamples B-1 to B-4 were separated by dissolving gypsum in weak acid (1N HNO_3). The other separates were processed using a magnetic mineral separator.

Table A.1
Radiocarbon ages for E-19 and Laguna del Perro (LDP) deflation basin outcrop exposures (from Allen and Anderson, 2000).

^{14}C age (yr B.P.)	Error (1σ)	AMS lab number	Material	Locality	Stratigraphic level (m)*
12490	60	CAMS-26397	Ostracodes	E19	0.675
13020	60	CAMS-26474	Ostracodes	E19	0.95
13410	60	CAMS-26398	Ostracodes	E19	1.21
13840	60	CAMS-25413	Ostracodes	E19	1.35
15130	80	CAMS-4099	Ostracodes	E19	3.375
15260	60	CAMS-18616	Ostracodes	E19	3.275
15970	60	CAMS-18617	Ostracodes	E19	3.625
16770	60	CAMS-18614	Ostracodes	E19	3.85
17960	90	CAMS-4100	Ostracodes	E19	4.25
18430	60	CAMS-18615	Ostracodes	E19	4.475
18920	90	CAMS-16603	Ostracodes	E19	4.70
20080	100	CAMS-16602	Ostracodes	E19	4.95
20090	70	CAMS-18619	Pelecypods	E19	4.95
20980	80	CAMS-26791	Ostracodes	E19	5.80
21190	100	CAMS-16601	Ostracodes	E19	5.95
21490	100	CAMS-26792	Ostracodes	E19	6.10
22900	140	CAMS-25414	Ostracodes	E19	7.375
23290	100	CAMS-16608	Ostracodes	E19	7.55
24050	100	CAMS-26793	Ostracodes	E19	7.65
25460	100	CAMS-18620	Ostracodes	E19	7.825
28910	150	CAMS-18613	Ostracodes	LDP	8.773
31340	210	CAMS-18612	Ostracodes	LDP	9.286

*Stratigraphic level is determined relative to the gypsum and magnesite desiccation layer (B-zone layer of Bachhuber, 1971), which is here defined as the 0-m level. All stratigraphic levels represent increasing depth from this layer.

Table A.2
U-series results for gypsum and magnesite sand layers. B samples come from the B-zone gypsum and magnesite layer. E samples come from the Laguna del Perro E-zone outcrop. F samples come from the Laguna del Perro F-zone outcrop. CR samples come from the Laguna del Perro sediment core.

Sub-sample	Stratigraphic level (m)	^{238}U (ppb)	^{232}Th (ppt)	^{230}Th/^{232}Th activity	^{230}Th/^{238}U activity	$\delta^{234}U_{meas}$ (‰)	$\delta^{234}U_{initial}$ (‰)	Uncorrected age (yrs BP)	Corrected age (yrs BP)	Material analyzed	Instrument used
B-1	0	1719.3 ± 1.5	698274 ± 411	2.496 ± 0.005	0.332 ± 0.001	1033 ± 2	1072 ± 5	19146 ± 50	13313 ± 1434	Magnesite separate	MC-ICPMS
B-2	0	1810.6 ± 1.4	630076 ± 322	2.667 ± 0.006	0.304 ± 0.001	1035 ± 2	1072 ± 4	17388 ± 44	12406 ± 1228	Magnesite separate	MC-ICPMS
B-3	0	3370.1 ± 2.1	1335001 ± 691	2.463 ± 0.005	0.319 ± 0.001	1035 ± 2	1073 ± 5	18346 ± 46	12662 ± 1398	Magnesite separate	MC-ICPMS
B-4	0	3949.5 ± 2.8	1226732 ± 454	3.069 ± 0.006	0.312 ± 0.001	1043 ± 2	1083 ± 4	17821 ± 45	13407 ± 1090	Magnesite separate	MC-ICPMS
B-5	0	598.3 ± 1.4	310292 ± 760	2.18 ± 0.009	0.37 ± 0.001	974 ± 1	1014 ± 6	22260 ± 97	14542 ± 1889	Gypsum + magnesite	MC-ICPMS
B-6	0	114.7 ± 0.4	55489 ± 256	2.279 ± 0.065	0.361 ± 0.01	1037 ± 10	1079 ± 12	20909 ± 656	13953 ± 1813	Gypsum separate	TIMS
B-7	0	114.9 ± 1.3	55524 ± 531	2.339 ± 0.072	0.37 ± 0.012	1030 ± 45	1073 ± 47	21568 ± 919	14603 ± 1874	Gypsum separate	TIMS
B-8	0	94.1 ± 0.3	48783 ± 135	2.091 ± 0.055	0.355 ± 0.009	1027 ± 7	1066 ± 9	20634 ± 594	13119 ± 1922	Gypsum separate	TIMS
B-9	0	94.3 ± 0.3	47246 ± 2917	2.564 ± 0.24	0.42 ± 0.03	1040 ± 11	1093 ± 14	24677 ± 1930	17518 ± 2574	Gypsum separate	TIMS
B-10	0	94.7 ± 0.3	46247 ± 252	2.344 ± 0.201	0.375 ± 0.032	1028 ± 8	1072 ± 12	21903 ± 2060	14854 ± 2611	Gypsum separate	TIMS
B-11	0	94.7 ± 0.4	46236 ± 184	2.354 ± 0.079	0.376 ± 0.013	1036 ± 15	1080 ± 16	21898 ± 826	14881 ± 1886	Gypsum separate	TIMS
B-12	0	5592.2 ± 88.7	3279511 ± 47072	2.133 ± 0.042	0.409 ± 0.008	974 ± 15	1019 ± 17	24866 ± 610	16125 ± 2184	Magnesite separate	MC-ICPMS
B-13	0	6317.6 ± 40.1	3662002 ± 24893	2.245 ± 0.043	0.426 ± 0.008	968 ± 5	1017 ± 8	26059 ± 555	17412 ± 2169	Magnesite separate	TIMS
B-14	0	6308.6 ± 97.9	3682056 ± 31568	2.28 ± 0.054	0.435 ± 0.012	975 ± 14	1025 ± 16	26620 ± 832	17949 ± 2230	Magnesite separate	TIMS
B-15	0	6769.7 ± 36.3	3045305 ± 14555	2.238 ± 0.03	0.329 ± 0.004	984 ± 5	984 ± 5	19512 ± 289	12865 ± 1651	Magnesite separate	TIMS
B-16	0	6813.2 ± 89	3029251 ± 28161	2.235 ± 0.076	0.325 ± 0.011	977 ± 13	977 ± 13	19309 ± 748	12715 ± 1756	Magnesite separate	TIMS
							wt. average age* =		**13916 ± 850**	**95% confid.**	
F1-1	8.24	983.3 ± 1.3	76331 ± 97	21.463 ± 0.052	0.545 ± 0.001	1068 ± 2	1167 ± 4	32496 ± 97	31449 ± 1051	Gypsum sand	MC-ICPMS
F1-2	8.24	1182.2 ± 1	105135 ± 59	19.588 ± 0.041	0.57 ± 0.001	1074 ± 2	1179 ± 5	34054 ± 94	32861 ± 1197	Gypsum sand	MC-ICPMS
F1-3	8.24	698.2 ± 0.7	71757 ± 67	16.887 ± 0.038	0.568 ± 0.001	1074 ± 2	1178 ± 5	33915 ± 97	32534 ± 1384	Gypsum sand	MC-ICPMS
							wt. average age =		**32179 ± 690**	**2σ-internal**	
F2-1	8.79	211.6 ± 0.2	61738 ± 134	6.998 ± 0.021	0.668 ± 0.002	1110 ± 2	1230 ± 14	40107 ± 121	36243 ± 3866	Gypsum sand	MC-ICPMS
F2-2	8.79	236.6 ± 0.3	65904 ± 292	7.352 ± 0.04	0.67 ± 0.002	1108 ± 2	1229 ± 13	40294 ± 170	36605 ± 3693	Gypsum sand	MC-ICPMS
F2-3	8.79	231.6 ± 0.3	63469 ± 92	7.398 ± 0.019	0.664 ± 0.002	1145 ± 2	1266 ± 13	38997 ± 117	35429 ± 3570	Gypsum sand	MC-ICPMS
							wt. average age =		**36072 ± 2100**	**2σ-internal**	
F3-1	9.09	375.8 ± 0.9	39106 ± 100	19.226 ± 0.089	0.655 ± 0.003	1165 ± 1	1291 ± 2	37901 ± 201	36654 ± 385	Gypsum sand	MC-ICPMS
F3-2	9.09	163.8 ± 0.4	19201 ± 230	17.333 ± 0.266	0.665 ± 0.007	1160 ± 3	1288 ± 4	38693 ± 452	37277 ± 582	Gypsum sand	MC-ICPMS
F3-3	9.09	381.7 ± 0.9	49226 ± 134	15.671 ± 0.076	0.661 ± 0.003	1158 ± 2	1284 ± 3	38494 ± 213	36924 ± 461	Gypsum sand	MC-ICPMS
F3-4	9.09	1947.5 ± 4.6	150789 ± 357	25.871 ± 0.1	0.655 ± 0.003	1153 ± 2	1281 ± 4	38291 ± 177	37300 ± 1007	Gypsum sand	MC-ICPMS
F3-5	9.09	1770.3 ± 4.3	157450 ± 386	22.956 ± 0.09	0.668 ± 0.003	1150 ± 2	1281 ± 5	39206 ± 184	38067 ± 1154	Gypsum sand	MC-ICPMS
F3-6	9.09	1823 ± 4.3	143842 ± 342	25.277 ± 0.098	0.653 ± 0.003	1153 ± 2	1280 ± 4	38087 ± 177	37076 ± 1026	Gypsum sand	MC-ICPMS
							wt. average age =		**36870 ± 260**	**2σ-internal**	
CR1-1	9.74	235 ± 0.2	26184 ± 144	21.592 ± 0.203	0.787 ± 0.006	1151 ± 2	1312 ± 6	47570 ± 447	46160 ± 1478	Gypsum sand	MC-ICPMS
CR1-2	9.74	284 ± 0.3	28766 ± 243	23.167 ± 0.216	0.768 ± 0.003	1153 ± 2	1309 ± 5	46135 ± 231	44852 ± 1303	Gypsum sand	MC-ICPMS
CR1-3	9.74	351.1 ± 0.3	43255 ± 214	18.69 ± 0.107	0.753 ± 0.002	1152 ± 2	1302 ± 6	45133 ± 174	43567 ± 1576	Gypsum sand	MC-ICPMS
							wt. average age =		**44908 ± 830**	**2σ-internal**	
CR2-1	10.66	816.8 ± 0.6	185640 ± 305	12.451 ± 0.033	0.926 ± 0.002	1075 ± 2	1266 ± 11	60917 ± 187	57965 ± 2958	Gypsum sand	MC-ICPMS
CR2-2	10.66	387.9 ± 0.3	105524 ± 208	10.374 ± 0.03	0.923 ± 0.002	1060 ± 2	1247 ± 13	61293 ± 195	57722 ± 3576	Gypsum sand	MC-ICPMS
CR2-3	10.66	794.4 ± 0.5	207300 ± 279	10.833 ± 0.027	0.925 ± 0.002	1067 ± 2	1256 ± 12	61140 ± 188	57730 ± 3415	Gypsum sand	MC-ICPMS
							wt. average age =		**57824 ± 1900**	**2σ-internal**	
CR3-1	11.15	238.9 ± 0.2	53090 ± 157	12.322 ± 0.051	0.896 ± 0.003	1077 ± 2	1260 ± 11	58352 ± 236	55458 ± 2903	Gypsum sand	MC-ICPMS
CR3-2	11.15	281.8 ± 0.2	84027 ± 339	9.802 ± 0.048	0.956 ± 0.003	1076 ± 2	1273 ± 14	63408 ± 248	59535 ± 3880	Gypsum sand	MC-ICPMS
CR3-3	11.15	481.5 ± 0.3	134557 ± 547	10.52 ± 0.048	0.962 ± 0.002	1082 ± 2	1282 ± 13	63652 ± 198	60040 ± 3617	Gypsum sand	MC-ICPMS

Table A.2 (*continued*)

Sub-sample	Stratigraphic level (m)	^{238}U (ppb)	^{232}Th (ppt)	^{230}Th/^{232}Th activity	^{230}Th/^{238}U activity	$\delta^{234}U_{meas}$ (‰)	$\delta^{234}U_{initial}$ (‰)	Uncorrected age (yrs BP)	Corrected age (yrs BP)	Material analyzed	Instrument used
							wt. average age =		**59833 ± 2000**	**2σ-internal**	
CR4-1	11.71	489.7 ± 0.3	144807 ± 442	10.415 ± 0.072	1.008 ± 0.006	1112 ± 2	1327 ± 14	66312 ± 544	62561 ± 3789	Gypsum sand	MC-ICPMS
CR4-2	11.71	563 ± 0.4	135176 ± 294	12.85 ± 0.039	1.01 ± 0.002	1119 ± 2	1337 ± 12	66190 ± 211	63167 ± 3031	Gypsum sand	MC-ICPMS
CR4-3	11.71	635.9 ± 0.6	146423 ± 136	13.795 ± 0.031	1.039 ± 0.002	1127 ± 2	1356 ± 11	68376 ± 221	65501 ± 2883	Gypsum sand	MC-ICPMS
							wt. average age =		**63966 ± 1800**	**2σ-internal**	
Analyses used to determine the initial ^{230}Th/^{232}Th value									^{230}Th/^{232}Th$_i$ age measured		
E1-1	3.51	135.5 ± 0.4	215399 ± 525	1.098 ± 0.009	0.572 ± 0.005	784 ± 4	826 ± 5	40881 ± 415	18285 3.590E-06	Gypsum sand	MC-ICPMS
E1-2	3.51	230.7 ± 0.3	357637 ± 402	1.200 ± 0.003	0.609 ± 0.002	627 ± 2	660 ± 3	49457 ± 164	18323 4.460E-06	Gypsum sand	MC-ICPMS
E1-3	3.51	94.0 ± 0.2	147876 ± 607	1.332 ± 0.009	0.686 ± 0.004	811 ± 3	854 ± 37	49948 ± 392	18318 4.990E-06	Gypsum sand	MC-ICPMS
E2-1	4.10	407.5 ± 1.0	1087381 ± 2475	1.078 ± 0.004	0.941 ± 0.004	756 ± 1	804 ± 5	78376 ± 427	21754 4.670E-06	Gypsum sand	MC-ICPMS
							average initial ^{230}Th/^{232}Th =		4.428E-06		

*Several U-series ages per sample were weight-averaged using Isoplot (Ludwig, 2000), which gives higher statistical weights to analyses with lower error ranges. All errors are reported as 2σ. Correction of ages was based on a ^{230}Th/^{232}Th atomic ratio = $4.4 \times 10^{-6} \pm 100\%$, which was measured using four analyses of two gypsum sand layers that had low U/Th (E1 and E2) where the ^{14}C chronology was highly resolved in the E-zone. Sample sizes ranged from 25 to 220 mg. TIMS = thermal ionization mass spectrometry and MC-ICPMS = multicollector inductively coupled plasma mass spectrometry. Stratigraphic level is determined relative to the gypsum and magnesite desiccation layer (B-zone layer of Bachhuber, 1971), which is here defined as the 0-m level. All stratigraphic levels represent increasing depth from this layer.

Table A.3
Combined outcrop and core HBI series. Ages determined via COPRA. Stratigraphic zones from Bachhuber (1971).

Zone	Age (yr BP)	Depth (m)	HBI	Zone	Age (yr BP)	Depth (m)	HBI
B	13670	0.00	3.5	C	15621	0.97	4.5
C	13709	0.03	3.5	C	15677	1.00	4.5
C	13749	0.05	3.5	C	15733	1.02	3.5
C	13788	0.07	3.5	C	15788	1.05	3.0
C	13828	0.10	3.5	C	15844	1.08	4.0
C	13867	0.13	3.5	C	15900	1.10	4.5
C	13907	0.15	2.5	C	15955	1.13	4.5
C	13946	0.17	2.0	C	16011	1.15	5.0
C	13986	0.20	1.5	C	16067	1.18	5.0
C	14025	0.23	2.0	C	16122	1.20	5.0
C	14065	0.25	2.5	C	16212	1.23	4.5
C	14104	0.28	3.5	C	16324	1.25	4.5
C	14144	0.30	4.0	C	16437	1.27	4.5
C	14183	0.33	3.5	C	16549	1.30	5.0
C	14223	0.35	1.5	C	16662	1.33	5.0
C	14262	0.38	1.0	C	16774	1.35	5.0
C	14302	0.40	1.5	D	16794	1.38	4.5
C	14341	0.42	2.0	D	16814	1.40	4.0
C	14381	0.45	1.5	D	16834	1.43	3.5
C	14420	0.47	2.0	D	16854	1.45	4.0
C	14460	0.50	2.0	D	16874	1.48	4.5
C	14499	0.53	1.5	D	16878	1.48	2.0
C	14539	0.55	4.0	D	16882	1.49	2.0
C	14578	0.57	4.5	D	16886	1.49	1.5
C	14618	0.60	3.5	D	16890	1.50	1.5
C	14657	0.63	3.5	D	16892	1.50	1.0
C	14697	0.65	4.0	D	16894	1.50	1.0
C	14736	0.68	4.0	D	16894	1.50	2.0
C	14812	0.70	4.0	D	16914	1.52	4.5
C	14887	0.72	4.0	D	16934	1.55	4.5
C	14962	0.75	4.5	D	16954	1.58	2.0
C	15038	0.78	5.0	D	16974	1.60	1.5
C	15113	0.80	5.0	D	16995	1.63	1.0
C	15189	0.82	3.5	D	17015	1.65	1.0
C	15264	0.85	4.5	D	17035	1.68	1.5
C	15339	0.88	4.0	D	17055	1.70	1.0
C	15415	0.90	4.5	D	17075	1.73	1.0
C	15490	0.93	3.5	D	17095	1.75	1.0
C	15566	0.95	4.5	D	17115	1.77	1.5
D	17135	1.80	2.0	D	17937	2.80	1.0
D	17155	1.83	1.5	D	17957	2.83	1.0
D	17175	1.85	1.0	D	17977	2.85	1.5
D	17195	1.88	1.0	D	17997	2.88	1.5
D	17215	1.90	1.0	D	18017	2.90	1.5
D	17235	1.93	1.5	D	18037	2.92	1.0
D	17255	1.95	1.0	D	18057	2.95	1.0
D	17275	1.98	1.0	D	18077	2.98	1.0

Table A.3 (*continued*)

Zone	Age (yr BP)	Depth (m)	HBI	Zone	Age (yr BP)	Depth (m)	HBI
D	17295	2.00	1.0	D	18097	3.00	1.0
D	17315	2.02	1.5	D	18117	3.02	1.0
D	17335	2.05	1.5	D	18137	3.05	1.0
D	17355	2.08	1.5	D	18157	3.08	1.0
D	17375	2.10	2.0	D	18177	3.10	1.5
D	17395	2.13	2.0	D	18197	3.13	1.0
D	17415	2.15	1.0	D	18217	3.15	2.0
D	17435	2.17	1.5	D	18237	3.17	3.5
D	17456	2.20	2.0	D	18257	3.20	3.5
D	17476	2.23	1.5	D	18277	3.23	3.0
D	17496	2.25	1.0	D	18297	3.25	3.0
D	17516	2.27	1.0	D	18317	3.27	4.0
D	17536	2.30	1.0	D	18337	3.30	3.5
D	17556	2.33	1.0	D	18357	3.33	3.0
D	17576	2.35	1.5	D	18378	3.35	3.0
D	17596	2.38	1.5	D	18398	3.38	3.0
D	17616	2.40	1.5	E	18486	3.40	3.0
D	17636	2.42	1.0	E	18574	3.42	3.0
D	17656	2.45	1.0	E	18662	3.45	3.0
D	17676	2.48	1.5	E	18751	3.48	3.5
D	17696	2.50	1.5	E	18839	3.50	3.5
D	17716	2.52	1.0	E	18927	3.52	3.0
D	17736	2.55	1.0	E	19016	3.55	3.0
D	17756	2.58	2.0	E	19104	3.58	3.0
D	17776	2.60	2.0	E	19192	3.60	3.0
D	17796	2.63	2.0	E	19280	3.63	3.0
D	17816	2.65	2.0	E	19387	3.65	3.0
D	17836	2.67	1.5	E	19493	3.67	3.0
D	17856	2.70	1.0	E	19599	3.70	3.0
D	17876	2.73	1.5	E	19705	3.73	3.5
D	17896	2.75	1.0	E	19799	3.75	4.0
D	17917	2.77	1.5	E	19906	3.77	4.0
E	20013	3.80	4.0	E	23479	4.83	2.0
E	20120	3.83	5.0	E	23614	4.85	2.0
E	20227	3.85	5.0	E	23749	4.88	2.0
E	20323	3.88	5.0	E	23884	4.90	2.0
E	20418	3.90	4.0	E	24018	4.92	2.0
E	20514	3.92	4.0	E	24153	4.95	2.0
E	20609	3.95	5.0	F	24185	4.97	2.0
E	20705	3.98	5.0	F	24217	5.00	2.0
E	20800	4.00	5.0	F	24249	5.03	1.5
E	20896	4.03	5.0	F	24281	5.05	1.5
E	20991	4.05	5.0	F	24313	5.08	2.0
E	21087	4.08	4.0	F	24345	5.10	2.0
E	21182	4.10	5.0	F	24377	5.13	1.5
E	21278	4.13	5.0	F	24409	5.15	2.0
E	21373	4.15	5.0	F	24441	5.17	3.0
E	21469	4.17	5.0	F	24473	5.20	4.5
E	21564	4.20	5.0	F	24505	5.22	3.5

(*continued on next page*)

Table A.3 (*continued*)

Zone	Age (yr BP)	Depth (m)	HBI	Zone	Age (yr BP)	Depth (m)	HBI
E	21660	4.22	5.0	F	24537	5.25	2.5
E	21755	4.25	5.0	F	24569	5.28	2.5
E	21817	4.28	5.0	F	24601	5.30	3.0
E	21880	4.30	5.0	F	24632	5.33	3.5
E	21942	4.33	5.0	F	24664	5.35	4.0
E	22004	4.35	5.0	F	24696	5.38	3.0
E	22066	4.38	5.0	F	24728	5.40	2.0
E	22128	4.40	3.5	F	24760	5.42	2.5
E	22190	4.42	3.0	F	24792	5.45	3.5
E	22252	4.45	4.0	F	24824	5.47	3.0
E	22314	4.47	4.5	F	24856	5.50	2.5
E	22369	4.50	4.5	F	24888	5.53	2.0
E	22424	4.53	4.5	F	24920	5.55	2.0
E	22478	4.55	4.5	F	24952	5.58	1.5
E	22533	4.58	4.5	F	24984	5.60	2.0
E	22587	4.60	4.5	F	25016	5.63	2.0
E	22642	4.63	4.0	F	25048	5.65	2.5
E	22696	4.65	4.0	F	25080	5.67	2.5
E	22751	4.67	4.0	F	25112	5.70	2.5
E	22805	4.70	4.0	F	25144	5.72	2.0
E	22940	4.72	3.0	F	25176	5.75	4.0
E	23075	4.75	3.0	F	25208	5.78	5.0
E	23210	4.78	4.0	F	25239	5.80	4.5
E	23344	4.80	4.0	F	25290	5.83	3.0
F	25341	5.85	3.5	F	26638	6.88	4.0
F	25392	5.88	3.0	F	26664	6.90	3.5
F	25442	5.90	3.5	F	26689	6.92	2.5
F	25493	5.92	4.5	F	26714	6.95	3.5
F	25544	5.95	5.0	F	26739	6.97	2.5
F	25596	5.97	2.0	F	26764	7.00	2.0
F	25649	6.00	5.0	F	26789	7.03	3.5
F	25701	6.03	4.5	F	26815	7.05	2.0
F	25753	6.05	2.0	F	26840	7.08	3.5
F	25806	6.08	2.0	F	26865	7.10	3.0
F	25858	6.10	2.0	F	26890	7.13	2.5
F	25883	6.13	2.0	F	26915	7.15	2.0
F	25909	6.15	2.0	F	26940	7.17	3.5
F	25934	6.17	2.0	F	26966	7.20	2.5
F	25959	6.20	2.0	F	26991	7.22	4.0
F	25984	6.22	2.0	F	27016	7.25	2.5
F	26009	6.25	2.5	F	27041	7.28	2.0
F	26034	6.28	3.5	F	27066	7.30	3.5
F	26060	6.30	4.0	F	27091	7.33	3.5
F	26085	6.33	3.5	F	27117	7.35	4.0
F	26110	6.35	5.0	F	27142	7.38	4.5
F	26135	6.38	5.0	F	27201	7.40	5.0
F	26160	6.40	4.5	F	27261	7.42	3.5
F	26185	6.42	4.5	F	27321	7.45	2.5
F	26211	6.45	4.5	F	27381	7.47	4.0
F	26236	6.47	5.0	F	27440	7.50	4.0
F	26261	6.50	4.5	F	27500	7.53	4.5
F	26286	6.53	4.5	F	27560	7.55	5.0
F	26311	6.55	4.5	F	27697	7.58	5.0
F	26336	6.58	4.5	F	27835	7.60	4.5
F	26362	6.60	3.5	F	27973	7.63	5.0
F	26387	6.63	3.5	F	28000	7.63	4.5
F	26412	6.65	4.5	F	28055	7.64	4.0
F	26437	6.67	4.5	F	28110	7.65	4.0
F	26462	6.70	4.0	F	28192	7.66	4.0
F	26487	6.72	4.5	F	28275	7.67	4.0
F	26513	6.75	3.5	F	28357	7.68	4.0
F	26538	6.78	4.5	F	28439	7.69	4.0
F	26563	6.80	2.5	F	28521	7.70	3.5
F	26588	6.83	2.5	F	28604	7.71	3.0
F	26613	6.85	3.5	F	28686	7.72	3.0
F	28768	7.73	3.0	F	31541	8.14	3.0
F	28851	7.74	3.5	F	31604	8.15	3.0
F	28933	7.75	3.0	F	31667	8.16	3.0
F	29015	7.76	3.5	F	31731	8.17	3.0
F	29097	7.77	3.5	F	31794	8.18	3.0
F	29180	7.78	4.0	F	31857	8.19	3.0
F	29262	7.79	4.5	F	31920	8.20	3.0
F	29344	7.80	4.5	F	31983	8.21	3.0
F	29427	7.81	4.5	F	32047	8.22	3.0

Table A.3 (*continued*)

Zone	Age (yr BP)	Depth (m)	HBI	Zone	Age (yr BP)	Depth (m)	HBI
F	29509	7.82	4.0	F	32110	8.23	3.0
F	29582	7.83	4.0	F	32169	8.24	3.5
F	29645	7.84	3.5	F	32223	8.25	4.0
F	29708	7.85	3.5	F	32276	8.26	4.0
F	29771	7.86	3.0	F	32330	8.27	4.0
F	29834	7.87	3.0	F	32383	8.28	4.0
F	29898	7.88	3.0	F	32437	8.29	4.5
F	29961	7.89	3.0	F	32490	8.30	4.5
F	30024	7.90	3.0	F	32544	8.31	4.5
F	30087	7.91	3.5	F	32597	8.32	4.5
F	30150	7.92	3.0	F	32651	8.33	4.5
F	30214	7.93	3.0	F	32704	8.34	4.0
F	30277	7.94	3.5	F	32758	8.35	3.5
F	30340	7.95	3.5	F	32811	8.36	3.5
F	30403	7.96	3.5	F	32865	8.37	4.0
F	30466	7.97	3.0	F	32918	8.38	4.0
F	30530	7.98	3.0	F	32972	8.39	2.0
F	30593	7.99	3.0	F	33025	8.40	2.0
F	30656	8.00	3.5	F	33079	8.41	2.0
F	30719	8.01	3.5	F	33132	8.42	2.5
F	30782	8.02	3.5	F	33186	8.43	3.5
F	30846	8.03	3.0	F	33239	8.44	3.5
F	30909	8.04	3.0	F	33293	8.45	3.5
F	30972	8.05	3.0	F	33346	8.46	4.0
F	31035	8.06	3.0	F	33400	8.47	4.0
F	31098	8.07	3.0	F	33453	8.48	3.5
F	31162	8.08	3.0	F	33507	8.49	2.5
F	31225	8.09	3.0	F	33560	8.50	3.5
F	31288	8.10	2.5	F	33614	8.51	3.5
F	31351	8.11	2.5	F	33667	8.52	3.0
F	31414	8.12	2.5	F	33721	8.53	2.5
F	31478	8.13	3.0	F	33775	8.54	2.0
F	33828	8.55	2.0	F	36131	8.96	4.0
F	33882	8.56	2.0	F	36190	8.97	2.0
F	33935	8.57	2.5	F	36250	8.98	2.0
F	33989	8.58	2.5	F	36310	8.99	1.5
F	34042	8.59	3.0	F	36370	9.00	1.5
F	34096	8.60	4.5	F	36429	9.01	2.0
F	34149	8.61	4.5	F	36489	9.02	2.5
F	34203	8.62	4.5	F	36549	9.03	2.5
F	34256	8.63	3.5	F	36609	9.04	2.5
F	34310	8.64	3.5	F	36668	9.05	2.0
F	34363	8.65	3.5	F	36728	9.06	2.0
F	34417	8.66	4.0	F	36788	9.07	3.0
F	34470	8.67	4.5	F	36847	9.08	3.5
F	34524	8.68	4.5	F	36932	9.09	4.5
F	34577	8.69	4.0	F	37054	9.10	4.0
F	34631	8.70	4.0	F	37176	9.11	4.5
F	34684	8.71	4.0	F	37297	9.12	5.0
F	34738	8.72	3.5	F	37419	9.13	4.5
F	34791	8.73	3.5	F	37541	9.14	4.0
F	34845	8.74	2.5	F	37663	9.15	4.0
F	34898	8.75	2.5	F	37784	9.16	4.5
F	34952	8.76	2.5	F	37906	9.17	4.5
F	35005	8.77	2.0	F	38028	9.18	4.5
F	35059	8.78	3.0	F	38149	9.19	4.5
F	35115	8.79	3.5	F	38271	9.20	4.0
F	35175	8.80	3.5	F	38393	9.21	3.5
F	35234	8.81	3.0	F	38515	9.22	5.0
F	35294	8.82	3.0	F	38636	9.23	4.5
F	35354	8.83	3.0	F	38758	9.24	4.5
F	35414	8.84	2.5	F	38880	9.25	4.5
F	35473	8.85	2.0	F	39002	9.26	4.5
F	35533	8.86	2.0	F	39123	9.27	5.0
F	35593	8.87	3.5	F	39245	9.28	4.5
F	35653	8.88	4.0	F	39367	9.29	4.5
F	35712	8.89	5.0	F	39489	9.30	4.0
F	35772	8.90	4.5	F	39610	9.31	4.0
F	35832	8.91	4.0	F	39732	9.32	3.0
F	35892	8.92	4.0	F	39854	9.33	3.0
F	35951	8.93	4.0	F	39976	9.34	2.5
F	36011	8.94	4.5	F	40097	9.35	3.0
F	36071	8.95	4.5	F	40219	9.36	3.0
F	40341	9.37	3.0	core	45384	9.78	4.5

Table A.3 (*continued*)

Zone	Age (yr BP)	Depth (m)	HBI	Zone	Age (yr BP)	Depth (m)	HBI
F	40463	9.38	3.5	core	45519	9.79	5.0
F	40584	9.39	4.5	core	45655	9.80	5.0
F	40706	9.40	5.0	core	45791	9.81	5.0
F	40828	9.41	5.0	core	45927	9.82	5.0
F	40950	9.42	5.0	core	46063	9.83	5.0
F	41071	9.43	4.5	core	46198	9.84	4.0
F	41193	9.44	4.5	core	46334	9.85	4.0
F	41315	9.45	4.5	core	46470	9.86	4.0
F	41437	9.46	5.0	core	46606	9.87	4.0
F	41558	9.47	5.0	core	46741	9.88	4.5
F	41680	9.48	4.5	core	46877	9.89	5.0
F	41802	9.49	5.0	core	47013	9.90	5.0
F	41924	9.50	5.0	core	47149	9.91	4.5
F	42045	9.51	4.5	core	47285	9.92	4.5
F	42167	9.52	3.5	core	47420	9.93	4.5
F	42289	9.53	4.0	core	47556	9.94	5.0
F	42411	9.54	4.0	core	47692	9.95	5.0
F	42532	9.55	4.0	core	47828	9.96	5.0
F	42654	9.56	5.0	core	47963	9.97	5.0
F	42776	9.57	4.5	core	48099	9.98	4.5
F	42898	9.58	4.0	core	48235	9.99	4.5
F	43019	9.59	2.5	core	48371	10.00	4.0
core	43141	9.60	2.0	core	48506	10.01	2.5
core	43263	9.61	2.0	core	48642	10.02	1.5
core	43385	9.62	2.0	core	48778	10.03	1.5
core	43506	9.63	1.0	core	48914	10.04	1.5
core	43628	9.64	1.0	core	49050	10.05	1.5
core	43750	9.65	2.0	core	49185	10.06	3.5
core	43872	9.66	2.0	core	49321	10.07	4.0
core	43993	9.67	2.0	core	49457	10.08	4.5
core	44115	9.68	2.0	core	49593	10.09	4.0
core	44237	9.69	1.5	core	49728	10.10	4.0
core	44359	9.70	1.5	core	49864	10.11	3.5
core	44480	9.71	1.0	core	50000	10.12	3.5
core	44602	9.72	1.0	core	50136	10.13	2.5
core	44724	9.73	1.0	core	50272	10.14	2.5
core	44846	9.74	1.0	core	50407	10.15	4.0
core	44976	9.75	1.0	core	50543	10.16	4.0
core	45112	9.76	1.0	core	50679	10.17	4.0
core	45248	9.77	1.5	core	50815	10.18	4.0
core	50950	10.19	4.0	core	56517	10.60	2.0
core	51086	10.20	3.5	core	56653	10.61	1.0
core	51222	10.21	2.0	core	56789	10.62	1.5
core	51358	10.22	2.0	core	56924	10.63	1.5
core	51493	10.23	2.0	core	57060	10.64	1.5
core	51629	10.24	2.0	core	57196	10.65	1.0
core	51765	10.25	1.5	core	57300	10.66	1.0
core	51901	10.26	1.0	core	57359	10.67	1.5
core	52037	10.27	1.5	core	57418	10.68	1.5
core	52172	10.28	2.0	core	57477	10.69	1.0
core	52308	10.29	1.5	core	57536	10.70	3.5
core	52444	10.30	2.0	core	57595	10.71	4.0
core	52580	10.31	2.0	core	57655	10.72	4.0
core	52715	10.32	1.5	core	57714	10.73	4.0
core	52851	10.33	1.0	core	57773	10.74	4.0
core	52987	10.34	1.0	core	57832	10.75	1.0
core	53123	10.35	1.0	core	57891	10.76	1.5
core	53259	10.36	1.0	core	57950	10.77	2.0
core	53394	10.37	1.5	core	58009	10.78	2.0
core	53530	10.38	1.0	core	58068	10.79	2.0
core	53666	10.39	1.5	core	58128	10.80	3.5
core	53802	10.40	2.0	core	58187	10.81	4.0
core	53937	10.41	2.0	core	58246	10.82	3.5
core	54073	10.42	2.0	core	58305	10.83	3.5
core	54209	10.43	2.0	core	58364	10.84	4.0
core	54345	10.44	2.0	core	58423	10.85	4.0
core	54480	10.45	1.5	core	58482	10.86	3.5
core	54616	10.46	1.5	core	58541	10.87	3.5
core	54752	10.47	1.5	core	58601	10.88	3.5
core	54888	10.48	1.5	core	58660	10.89	3.5
core	55024	10.49	1.0	core	58719	10.90	2.5
core	55159	10.50	1.0	core	58778	10.91	4.0
core	55295	10.51	1.0	core	58837	10.92	3.5
core	55431	10.52	1.0	core	58896	10.93	1.5
core	55567	10.53	1.0	core	58955	10.94	2.5

Table A.3 (*continued*)

Zone	Age (yr BP)	Depth (m)	HBI	Zone	Age (yr BP)	Depth (m)	HBI
core	55702	10.54	1.0	core	59014	10.95	3.5
core	55838	10.55	2.0	core	59074	10.96	3.5
core	55974	10.56	2.0	core	59133	10.97	2.5
core	56110	10.57	2.0	core	59192	10.98	1.0
core	56246	10.58	2.0	core	59251	10.99	1.0
core	56381	10.59	2.0	core	59310	11.00	1.5
core	59369	11.01	1.5	core	62166	11.42	3.5
core	59428	11.02	1.0	core	62238	11.43	2.5
core	59487	11.03	1.0	core	62311	11.44	1.5
core	59547	11.04	1.0	core	62384	11.45	1.0
core	59606	11.05	4.0	core	62456	11.46	2.0
core	59665	11.06	4.0	core	62529	11.47	3.0
core	59724	11.07	3.5	core	62602	11.48	3.0
core	59783	11.08	1.5	core	62674	11.49	4.0
core	59842	11.09	1.5	core	62747	11.50	4.0
core	59901	11.10	2.0	core	62820	11.51	4.0
core	59960	11.11	2.0	core	62892	11.52	4.0
core	60020	11.12	2.0	core	62965	11.53	3.5
core	60079	11.13	1.5	core	63038	11.54	3.5
core	60138	11.14	1.5	core	63110	11.55	3.5
core	60203	11.15	1.5	core	63183	11.56	3.5
core	60276	11.16	1.5	core	63256	11.57	1.0
core	60348	11.17	2.5	core	63329	11.58	1.5
core	60421	11.18	3.5	core	63401	11.59	1.0
core	60494	11.19	3.5	core	63474	11.60	1.0
core	60566	11.20	2.0	core	63547	11.61	1.0
core	60639	11.21	2.5	core	63619	11.62	1.0
core	60712	11.22	2.0	core	63692	11.63	3.0
core	60784	11.23	2.5	core	63765	11.64	1.5
core	60857	11.24	1.5	core	63837	11.65	1.0
core	60930	11.25	1.0	core	63910	11.66	1.5
core	61002	11.26	2.5	core	63983	11.67	3.0
core	61075	11.27	3.0	core	64055	11.68	2.5
core	61148	11.28	3.5	core	64128	11.69	2.0
core	61221	11.29	2.0	core	64201	11.70	1.0
core	61293	11.30	2.5	core	64273	11.71	1.0
core	61366	11.31	1.5	core	64346	11.72	1.0
core	61439	11.32	3.5	core	64419	11.73	1.0
core	61511	11.33	4.0	core	64492	11.74	1.0
core	61584	11.34	4.0	core	64564	11.75	1.5
core	61657	11.35	3.5	core	64637	11.76	2.5
core	61729	11.36	4.0	core	64710	11.77	3.0
core	61802	11.37	3.5	core	64782	11.78	3.5
core	61875	11.38	4.0	core	64855	11.79	4.0
core	61947	11.39	4.0	core	64928	11.80	4.0
core	62020	11.40	3.5	core	65000	11.81	2.5
core	62093	11.41	3.5	core	65073	11.82	1.5
core	65146	11.83	1.0	core	68126	12.24	2.0
core	65218	11.84	4.0	core	68199	12.25	2.0
core	65291	11.85	4.0	core	68271	12.26	2.0
core	65364	11.86	3.5	core	68344	12.27	3.0
core	65437	11.87	2.5	core	68417	12.28	3.5
core	65509	11.88	2.0	core	68489	12.29	4.0
core	65582	11.89	3.5	core	68562	12.30	4.0
core	65655	11.90	3.5	core	68635	12.31	4.0
core	65727	11.91	2.5	core	68708	12.32	4.0
core	65800	11.92	1.5	core	68780	12.33	3.0
core	65873	11.93	2.0	core	68853	12.34	3.5
core	65945	11.94	3.5	core	68926	12.35	3.5
core	66018	11.95	5.0	core	68998	12.36	3.0
core	66091	11.96	4.0	core	69071	12.37	3.5
core	66163	11.97	4.0	core	69144	12.38	3.5
core	66236	11.98	3.5				
core	66309	11.99	4.5				
core	66381	12.00	4.5				
core	66454	12.01	4.5				
core	66527	12.02	4.0				
core	66600	12.03	4.0				
core	66672	12.04	4.0				
core	66745	12.05	4.0				
core	66818	12.06	4.0				
core	66890	12.07	3.5				
core	66963	12.08	3.5				

(*continued on next page*)

Table A.3 (*continued*)

Zone	Age (yr BP)	Depth (m)	HBI	Zone	Age (yr BP)	Depth (m)	HBI
core	67036	12.09	3.5				
core	67108	12.10	3.0				
core	67181	12.11	3.0				
core	67254	12.12	3.0				
core	67326	12.13	3.0				
core	67399	12.14	3.0				
core	67472	12.15	2.5				
core	67544	12.16	2.0				
core	67617	12.17	2.5				
core	67690	12.18	2.5				
core	67763	12.19	2.5				
core	67835	12.20	3.0				
core	67908	12.21	3.5				
core	67981	12.22	2.5				
core	68053	12.23	2.0				

References

Allen, B.D., Anderson, R.Y., 1993. Evidence from western North America for rapid shifts in climate during the last glacial Maximum. Science 260, 1920–1923.

Allen, B.D., Anderson, R.Y., 2000. A continuous, high-resolution record of late Pleistocene climate variability from the Estancia basin, New Mexico. Geol. Soc. Am. Bull. 112, 1444–1458.

Allen, B.D., Love, D.W., Myers, R.G., 2009. Evidence for late Pleistocene hydrologic and climatic change from Lake Otero, Tularosa Basin, south-central New Mexico. N. M. Geol. 31, 9–25.

Anderson, R.Y., Allen, B.D., Menking, K.M., 2002. Geomorphic expression of abrupt climate change in southwestern North America at the glacial termination. Quat. Res. 57, 371–381.

Asmerom, Y., Polyak, V., Burns, S., Rassmussen, J., 2007. Solar forcing of Holocene climate: new insights from a speleothem record, southwestern United States. Geology 35, 1–4.

Asmerom, Y., Polyak, V., Burns, S.J., 2010. Variable winter moisture in the southwestern United States linked to rapid glacial climate shifts. Nat. Geosci. 3, 114–117.

Asmerom, Y., Polyak, V.J., Lachniet, M.S., 2017. Extrapolar climate reversal during the last deglaciation. Nature. https://doi.org/10.1038/s41598-017-07721-8.

Bachhuber, F.W., 1971. Paleolimnology of Lake Estancia and the Quaternary History of the Estancia Valley, Central New Mexico. PhD Dissertation. University of New Mexico, Albuquerque.

Ballenger, J.A.M., Holliday, V.T., Kowler, A.L., Reitze, W.T., Prasciunas, M.M., Miller, D.S., Windingstad, J.D., 2011. Evidence for Younger Dryas global climate oscillation and human response in the American Southwest. Quat. Int. 242, 502–519.

Baker, A., Hellstrom, J.C., Kelly, B.F.J., Mariethoz, G., Trouet, V., 2015. A composite annual-resolution stalagmite record of North Atlantic climate over the last three millennia. Sci. Rep. 5, 10307. https://doi.org/10.1038/srep10307.

Benson, L.V., Currey, D.R., Dorn, R.I., Lajoie, K.R., Oviatt, C.G., Robinson, S.W., Smith, G.I., Stine, S., 1990. Chronology of expansion and contraction of four Great Basin lake systems during the past 35,000 years. Palaeogeogr. Palaeoclimatol. Palaeoecol. 78, 241–286.

Benson, L.V., Lund, S.P., Smoot, J.P., Rhode, D.E., Spencer, R.J., Verosub, K.L., Louderback, L.A., Johnson, C.A., Rye, R.O., Negrini, R.M., 2011. The rise and fall of Lake Bonneville between 45 and 10.5 ka. Quat. Int. 235, 57–69.

Benson, L.V., Smoot, J.P., Lund, S.P., Mensing, S.A., Foit Jr., F.F., Rye, R.O., 2013. Insights from a synthesis of old and new climate-proxy data from the Pyramid and Winnemucca lake basins for the period 48 to 11.5 cal ka. Quat. Int. 310, 62–82.

Breitenbach, S.F.M., Rehfeld, K., Goswami, B., Baldini, J.U.L., Ridley, H.E., Kennett, D.J., Prufer, K.M., Aquino, V.V., Asmerom, Y., Polyak, V.J., Cheng, H., Kurths, J., Marwan, N., 2012. COnstructing Proxy Records from Age models (COPRA). Clim. Past 8, 1765–1779.

Broecker, W.S., McGee, D., Adams, K.D., Cheng, H., Edwards, R.L., Oviatt, C.G., Quade, J., 2009. A Great Basin-wide dry episode during the first half of the Mystery Interval. Quat. Sci. Rev. 28, 2557–2563.

Bryson, R.A., Hare, F.K., 1974. The climates of North America. In: Bryson, R.A., Hare, F.K. (Eds.), World Survey of Climatology, vol. 11. Elsevier Scientific Publishing Company, New York, pp. 1–47.

Cheng, H., Edwards, R.L., Shen, C.-C., Polyak, V.J., Asmerom, Y., Woodhead, J., Hellstrom, J., Wang, Y., Kong, X., Spötl, C., 2013. Improvements in 230 Th dating, 230 Th and 234 U half-life values, and U–Th isotopic measurements by multi-collector inductively coupled plasma mass spectrometry. Earth Planet Sci. Lett. 371, 82–91.

Feng, W., Hardt, B.F., Banner, J.L., Meyer, K.J., James, E.W., Musgrove, M., Edwards, R.L., Cheng, H., Min, A., 2014. Changing amounts and sources of moisture in the U.S. southwest since the Last Glacial Maximum in response to global climate change. Earth Planet Sci. Lett. 401, 47–56.

Hales Jr., J.E., 1974. Southwestern United States summer monsoon source—Gulf of Mexico or Pacific ocean? J. Appl. Meteorol. 13, 331–342.

Hall, S.A., Penner, W.L., Palacios-Fest, M.R., Metcalf, A.L., Smith, S.J., 2012. Cool, wet conditions late in the Younger Dryas in semi-arid New Mexico. Quat. Res. 77, 87–95.

Haynes Jr., C.V., 2008. Younger Dryas "black mats" and the Rancholabrean termination in North America. Proc. Natl. Acad. Sci. Unit. States Am. 105, 6520–6525.

Haynes Jr., C.V., Boerner, J., Domanik, K., Lauretta, D., Ballenger, J., Goreva, J., 2010. The Murray Springs Clovis site, Pleistocene extinction, and the question of extraterrestrial impact. Proc. Natl. Acad. Sci. Unit. States Am. 107, 4010–4015.

Huybers, P., Eisenman, I., 2006. Integrated summer insolation calculations. In: IGBP PAGES/World Data Center for Paleoclimatology Data Contribution Series # 2006-079. NOAA/NCDC Paleoclimatology Program, Boulder CO, USA.

Kutzbach, J.E., Wright, H.E., 1985. Simulation of the climate of 18,000 years B.P.: results for the North American/North Atlantic/European sector and comparison with the geological record of North America. Quat. Sci. Rev. 4, 147–187.

Ludwig, K.R., 2000. User's Manual for Isoplot/Ex Version 2.2. Berkeley Geochronology Center Special Publication No. 1a, Berkeley, CA.

Menking, K.M., Anderson, R.Y., 2003. Contributions of La Niña and El Niño to middle Holocene drought and late Holocene moisture in the American southwest. Geology 31, 937–940.

Menking, K.M., Anderson, R.Y., Shafike, N.G., Syed, K.H., Allen, B.D., 2004. Wetter or colder during the Last Glacial Maximum? Revisiting the pluvial lake question in southwestern North America. Quat. Res. 62, 280–288.

Menking, K.M., 2015. Decadal to millennial-scale solar forcing of last glacial Maximum climate in the Estancia basin of central New Mexico. Quat. Res. 83, 545–554.

Oviatt, C.G., Thompson, R.S., Kaufman, D.S., Bright, J., Forester, R.M., 1999. Reinterpretation of the Burmester core, Bonneville basin, Utah. Quat. Res. 52, 180–184.

Oviatt, C.G., 2015. Chronology of lake Bonneville, 30,000 to 10,000 yr B.P. Quat. Sci. Rev. 110, 166–171.

Polyak, V.J., Rasmussen, J.B.T., Asmerom, Y., 2004. Prolonged wet period in the southwestern United States through the Younger Dryas. Geology 32, 5–8.

Polyak, V.J., Asmerom, Y., 2005. Orbital control of long-term moisture in the southwestern USA. Geophys. Res. Lett. 32, 1–4. https://doi.org/10.1029/2005GL023919. L19709.

Polyak, V.J., Asmerom, Y., Burns, S.J., Lachniet, M.S., 2012. Climatic backdrop to the terminal Pleistocene extinction of North American mammals. Geology 40, 1023–1026.

Rasmussen, S.O., Bigler, M., Blockley, S.P., Blunier, T., Buchardt, S.L., Clausen, H.B., Cvijanovic, I., Dahl-Jensen, D., Johnsen, S.J., Fischer, H., Gkinis, V., Guillevic, M., Hoek, W.Z., Lowe, J.J., Pedro, J.B., Popp, T., Seierstad, I.K., Steffensen, J.P., Svensson, A.M., Vallelonga, P., Vinther, B.M., Walker, M.J.C., Wheatley, J.J., Winstrup, M., 2014. A stratigraphic framework for abrupt climatic changes during the Last Glacial period based on three synchronized Greenland ice-core records: refining and extending the INTIMATE event stratigraphy. Quat. Sci. Rev. 106, 14–28.

Seierstad, I.K., Abbott, P.M., Bigler, M., Blunier, T., Bourne, A.J., Brook, E., Buchardt, S.L., Buizert, C., Clausen, H.B., Cook, E., Dahl-Jensen, D., Davies, S.M., Guillevic, M., Johnsen, S.J., Pedersen, D.S., Popp, T.J., Rasmussen, S.O., Severinghaus, J.P., Svensson, A., Vinther, B.M., 2014. Consistently dated records from the Greenland GRIP, GISP2 and NGRIP ice cores for the past 104 ka reveal regional millennial-scale $\delta^{18}O$ gradients with possible Heinrich event imprint. Quat. Sci. Rev. 106, 29–46.

Steenburgh, W.J., Redmond, K.T., Kunkel, K.E., Doesken, N., Gillies, R.R., Horel, J.D., Hoerling, M.P., Painter, T.H., 2013. Present weather and climate: average conditions. In: Garfin, G., Jardine, A., Merideth, R., Black, M., LeRoy, S. (Eds.), Assessment of Climate Change in the Southwest United States: a Report Prepared for the National Climate Assessment. Island Press, Washington, DC, pp. 56–73. A report by the Southwest Climate Alliance.

Stuiver, M., Reimer, P.J., Reimer, R.W., 2018. CALIB 7.1 [WWW program] at: http://calib.org. accessed 2018-07-25.

Wagner, J.D.M., Cole, J.E., Beck, J.W., Patchett, P.J., Henderson, G.M., Barnett, H.R., 2010. Moisture variability in the southwestern United States linked to abrupt glacial climate change. Nat. Geosci. 3, 110–113.